Corrosion Fatigue Performance of Alloy 6013-T6

by

Jean-Marc P. Genkin

Ingénieur Civil, Ecole des Mines de Paris (1992)

Submitted to the Department of Materials Science and Engineering
in Partial Fulfillment of the Requirements for the Degree of
Master of Science in Materials Engineering

at

Massachusetts Institute of Technology

February 1994

© Massachusetts Institute of Technology

Signature of Author_____
Department of Materials Science and Engineering
January 14, 1994

Certified by_____
Professor Regis M.Pelloux
Thesis Advisor

Accepted by_____
Carl V.Thompson II
Professor of Electronic Materials
Chairman, Departmental Committee
on Graduate Students

MAR 02 1994

1

Corrosion Fatigue Performance of Alloy 6013-T6

by

Jean-Marc P.Genkin

Submitted to the Department of Materials Science and Engineering
on January 15, 1994 in Partial Fulfillment of the Requirements
for the Degree of Master of Science in Materials Engineering

ABSTRACT

In the context of the issue of aging airplanes, the FAA has initiated different research programs to study the effect of corrosion fatigue on the structural integrity of airplanes. 2024-T3 aluminum alloy is the alloy which has received the most attention since it is widely used by aircraft manufacturers. However, a few years ago, Alcoa introduced 6013-T6 aluminum alloy as a possible candidate to replace 2024-T3 in fuselage skin and leading edges. the research work reported here compares the fatigue performance of both alloys along with the effect of precorrosion on fatigue crack initiation and propagation lives in thin gauge aluminum alloys.

6013-T6 alclad microstructure is first studied to determine cladding thickness, grain size and second phase particles. Corrosion experiments are carried out by immersion in ASTM G69 solution. Maximum pit depth, pit area fraction and pit density are recorded. Pit diameter increases much slower than pit depth. Comparison with 2024-T3 alclad shows that pit density is much lower than in 2024-T3 alclad base metal but pits are deeper than in 6013-T6 alclad.

The fatigue performance of fuselage skin is simulated by using tensile specimens with a centered open hole. These specimens are precorroded for 6, 12 and 24 hours and fatigue tested in air at 10Hz, under a R-ratio of 0.05. Numerous pits are found on the walls of the open hole along with microcracks in the cladding and at the cladding/base metal interface. Fatigue crack initiation life is sharply reduced by precorrosion exposures. Comparison with 2024-T3 alclad shows that 6013-T6 alclad is inferior to 2024-T3 alclad in terms of fatigue performance, both in the as-received and in the precorroded conditions. The sensitivity of crack initiation life to precorrosion is higher in 6013-T6 alclad than in 2024-T3 alclad. For both alloys, increasing precorrosion times has little effect on fatigue performance. This can be attributed to the fact that the stress intensity factor at the tip of a pit varies very little with pit depth for a given pit diameter.

Fatigue crack growth tests are run at 10Hz under two different load ratios R=0.05, 0.33 to explore the influence of R-value on fatigue crack propagation. At a given ΔK, the crack growth rates are increased by a larger R-value. Precorroded and as-received specimens are used to evaluate the effect of corrosion damage on fatigue crack growth. No significant effect is recorded.
Fatigue crack growth tests run at 10Hz in ASTM G69 solution shows an increase in crack growth rates by a factor of 2 at low ΔK. Decreasing the frequency to 0.1 Hz decreases crack growth rates because of crack tip branching and blunting which lower the stress intensity at the tip of the crack.
It is concluded that corrosion fatigue damage in 6013-T6 alclad has a more detrimental effect on fatigue crack initiation than on fatigue crack propagation.

Thesis Supervisor: Regis M.Pelloux
Title: Professor of Materials Science and Engineering

TABLE OF CONTENTS

LIST OF FIGURES

5

LIST OF TABLES

ACKNOWLEDGMENT

I.1 Fatigue damage in aircraft structures

Damage by corrosion fatigue is probably the main structural damage factor that will affect the performance and the life of an airplane. However the severity of the degradation of an aircraft component by corrosion fatigue depends on its location in the airplane structure. Wings are subject to ground to air back to ground (G.A.C) cycles due to landing and take off and to fatigue cycles during the flight, due to the atmospheric perturbations and to plane maneuvers. On the contrary for the fuselage, the combination of a flight and a ground cycle corresponds to one single fatigue cycle. Tensile stresses are induced in the fuselage by the pressurization of the cabin. These stresses are relieved by depressurization during landing. An alternation of pressurization and depressurization constitutes one fatigue cycle. The loading time is typically 15 minutes corresponding to a strain rate of $4 \cdot 10^{-6}$ sec^{-1} with a nominal strain range of 0.25 %. The hold times at peak stress can vary from 1 hour to 10 hours.
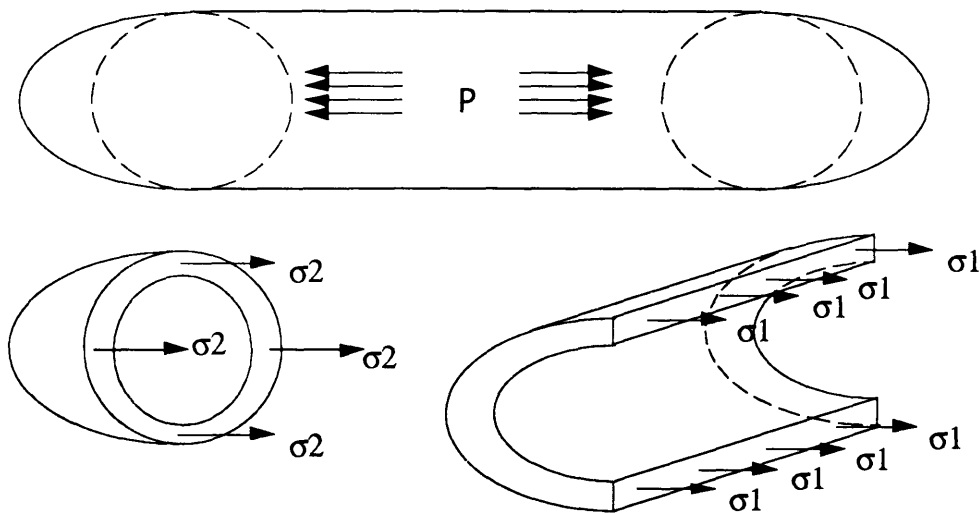
$\sigma 1$: hoop stress
$\sigma 2$: longitudinal stress
$\sigma 1 = 2 \, \sigma 2$

Fig.1.1: Fuselage modeled as a thin wall pressure vessel

Modeling the cabin as a cylindrical vessel with spherical ends, the highest stress is circumferential and is equal to twice the axial stress. It is in the order of 100 MPa or 15 ksi.

When corrosion takes place at the same time as fatigue, a synergistic effect is developed between the two degradation processes. Damage is enhanced. Corrosion fatigue is a serious issue for airplanes that are exposed to marine and/or polluted air. This environment is particularly detrimental to the corrosion fatigue performance of airplanes since chloride compounds induce the breakdown of the passive film which covers aluminum alloys and which protects them from the atmosphere.

In case of severe corrosion, fatigue cracks will initiate at each rivet. Since fatigue cracks propagate perpendicular to the direction of maximum tensile stress, the rivets rows, parallel to the axis of the plane, are a weak point in the airplane structure: multiple cracks at each rivet hole can coalesce suddenly to lead to a major failure of the skin. This has been called Multi Site Damage (MSD)[1] as seen on Fig.1.2:
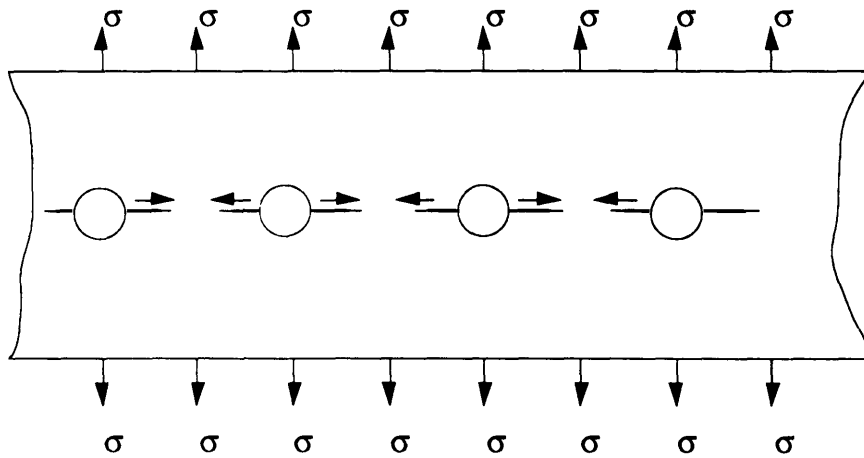
Fig.1.2: Multi Site Damage (MSD)

The issue of Multi site Damage (MSD) has been emphasized since the Aloha 737 accident. MSD is recognized as a characteristic phenomenon, different from the growth of an isolated fatigue crack. Actually, this particular damage is very difficult to predict

11

because the growth and coalescence of interacting cracks is very cumbersome to model: cracks can propagate in a non-collinear manner; the effect of large deformations must be accounted for when the fuselage bulge outwards under the effect of internal pressure; dynamic effects that may be present could enhance the crack driving force for cracks close to stress concentrators and further increase the overall crack velocity; in addition, in the case of a wide open crack, local stresses can be the result of a fluid/structure interaction (air leakage from fuselage); finally, the rapid crack propagation direction can change abruptly from axial to circumferential; in this case the crack arrest straps designed to avoid complete failure of the structure, may not work.

I.2 Aluminum used in the aircraft industry

I.2.1 Aluminum alloys classes: different applications

The aluminum alloys used in the aircraft industry essentially belong to the 1xxx series (commercially pure aluminum alloys), 2xxx series (Al-Cu-Mg aluminum alloys) and 7xxx series (Al-Zn-Mg-Cu aluminum alloys). Table 1 displays some examples of the applications of these alloys below:

Series	Examples	Applications
1xxx	1060	cladding
2xxx	2024-T3	fuselage skin
6xxx	6013-T6	fuselage skin / leading edges
7xxx	7075-T6/T8 7072	wing skin / fuselage skin (clad) cladding [2]

Table.1: Applications of aluminum alloys in the aircraft industry

I.2.2 Heat treatments: [3]

Heat treatment is used in the 2xxx, 6xxx and 7xxx aluminum alloys to develop precipitation strengthening. The heat treatments commonly used in the aircraft industry are T3, T4, T6 and T8. These heat treatments involve a solution treatment followed by an aging cycle. T3 and T8 also include some amount of cold work prior to the aging. T3 and T4 designate natural aging whereas T6 and T8 are for artificial aging.

Solution treatment dissolves most of the second phase particles formed by alloying elements. The aluminum alloys are then quenched. Cold work may be used to increase strength. Aging treatments develop strengthening precipitates. Those first to form are usually the Guinier-Preston zones. Further aging leads to the development of other precipitates whose shape, composition and coherency with respect to the matrix may be

different from the initial GP zones. If these precipitates differ from the equilibrium phase, they are called transition precipitates.

I.2.3 Second phase particles

In aluminum alloys three types of second phase particles are commonly observed: constituent particles, dispersoids and fine precipitates, as seen in Fig.1.3:

	fine precipitates
	dispersoids
	constituent particles
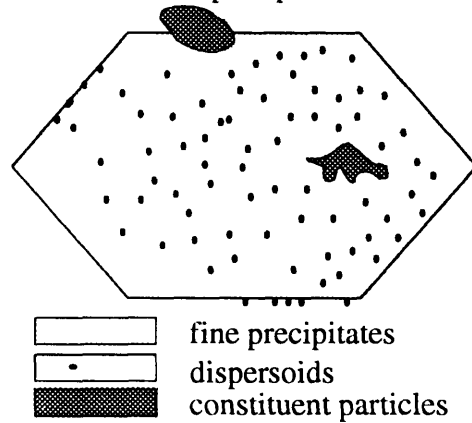
Fig.1.3: Second phases in an aluminum alloy

Constituent particles are first to be formed from the melt and contain the natural impurities of aluminum, silicon and iron. In addition, they may also include some alloying elements. Dispersoids are coarse precipitates in the order of micrometers. Fine precipitates are for example, the GP zones whose thickness is in the order of nanometers. During aging heat treatment, these GP zone evolve into other types of precipitates which are responsible for the strengthening of age hardenable aluminum alloys.

For instance, 6xxx series aluminum alloys are heat treatable medium strength alloys in which Mg_2Si is the precipitation hardening phase. In the absence of manganese or chromium, the iron rich phases are Fe_3SiAl_{12}, $FeSiAl_9$ or a mixture of the two. When manganese or chromium are present, the second phase particles are $(Fe, Mn, Cr)_3 Si Al_{12}$. [3]

I.2.4 6013-T6 aluminum alloy

a) Composition

Very few papers have been published about 6013 aluminum alloy. Alcoa introduced this alloy a few years ago and most of the investigations were carried out either by the Alcoa test laboratories or other private labs. According to Alcoa Green Letter 225 [4], 6013 nominal composition and tolerances are as follows in wt % :

Elements	Magnesium (Mg)	Silicon (Si)	Copper (Cu)	Manganese (Mn)	Iron (Fe)
Composition (wt%)	0.95	0.75	0.9	0.35	0.3
Tolerances (wt%)	0.8-1.2	0.6-1.0	0.6-1.1	0.2-0.8	0.5 max
Elements	Chromium(Cr)	Zinc(Zn)	Titanium (Ti)	Others (each)	Others (total)
Composition (wt%)	--	--	--	--	--
Tolerances (wt%)	0.1	0.25	0.1	0.05	0.15

Table 2 : Nominal chemical composition of 6013 alloy.

b) Phases

6013-T6 is an aluminum copper magnesium silicon alloy. No direct data is available about the strengthening mechanisms. However, alloy 6013-T6 does not fall in the high copper content group described by Mondolfo [5], since the copper content is well below 4 %. The remaining strengthening mechanisms are due to the precipitation of $Cu_2Mg_8Si_6Al_{15}$, $CuMgAl_2$ or Mg_2Si [5]. In the case of 6013 aluminum alloy case, Mg_2Si is the prevailing precipitate (aluminum-magnesium-silicon). Since iron and manganese form insoluble phases with copper and silicon [3], they consequently reduce the amounts of copper and silicon available for the aluminum-copper-magnesium-silicon phase reactions. According to Mondolfo [5], the alloying elements can be found in the following phases:

Manganese can be present only as $(Fe,Mn)_3Si_2Al_{15}$ since the magnesium content is not higher than twice the silicon content. It is supposed that this phase is the same as the one

15

reported in [3] and [5] as $(Fe,Mn)_3SiAl_{12}$ or as a variant of $(Fe,Mn)_3Si_2Al_{12}$. This phase may incorporate chromium in the iron-manganese sites and copper on the silicon sites. Silicon may be present as Mg_2Si, $Cu_2Mg_8Si_6Al_{15}$, $FeSiAl_5$ and $(Fe,Mn)_3Si_2Al_{15}$, mentionned above. But $FeSiAl_5$ which is similar to $Fe_2Si_2Al_9$ [2] is reported to transform into $(Fe,Mn)_3SiAl_{12}$ when Manganese and chromium are present [3]. Cu may be present as $CuMgAl_2$ and $Cu_2Mg_8Si_6Al_5$.

As a conclusion, the expected phases in 6013-T6 aluminum alloy are Mg_2Si, $CuMgAl_2$, $Cu_2Mg_8Si_6Al_5$ and $(Fe,Mn)_3SiAl_{12}$ or $(Fe,Mn)_3Si_2Al_{12}$.

c) Mechanical properties

Alloy 6013-T6 has a yield stress 12% higher than 2024-T3 alclad and 25% higher strength than 6061-T6 as seen in Table 3 [6]. Its density is 3% lower than the density of the aluminum alloys commonly used in the aircraft industry (2024 and 2014).

Series	Example	Thickness (mm)	Yield Strength	Tensile Strength
1xxx	1060	0.152-0.483	17 MPa	55-96 MPa
2xxx	2024 T3	0.203-6.32	289 MPa*	434-441 MPa *
6xxx	6013 T6	0.5-6.3	317 MPa*	359 MPa *
7xxx	7075 T6/T8	0.203-6.32	434-476 MPa (T6)*	510-538 MPa (T6)*

Table 3: Mechanical properties [6]

Excellent formability was reported in the T4 temper. Consequently, components could be formed in the T4 temper and simply aged to the T6 temper, avoiding costly heat treatments. 6013-T6 alloy is also weldable. In addition, Alcoa claims alloy 6013-T6 is corrosion resistant, but acknowledges that some intergranular corrosion may occur when the alloy is exposed to severe environments such as salt-water. It is expected that the new alloy is probably less resistant than 6061-T6 to intergranular corrosion. However, 6013-T6 has been found to be immune to stress corrosion cracking and exfoliation corrosion.[4]

16

6013-T6 alclad: Corrosion Fatigue Performance:[7]

It is reported [4] that general corrosion in 6013-T6 aluminum sheet follows a narrow intergranular path in salt-water type solutions. 2024 bare alloy exhibits slightly better corrosion fatigue performance than 6013-T6 which suffers from multiple cracking. A large data scatter for 6013-T6 specimens has been reported.

Aluminum Alloy 6013 Sheet for New US Navy Aircraft: [8]

6013-T6 aluminum alloy has been selected for the US's navy P-7A airplane in place of the traditionnal 2024-T3 clad sheet. The authors reported that the new alloy has significantly better fatigue performance, toughness, and roughly equivalent fatigue crack propagation resistance than 2024-T3.

I.3. Pitting of aluminum alloys.

Aluminum and its alloys are very active in the electrochemical series. The standard potential of pure aluminum, measured against the Standard Hydrogen Electrode (SHE) is -1.662 V at 25°C. The Pourbaix diagram [9] for aluminum shows that alumina (Al_2O_3) is the stable form of aluminum between pH 4 and pH 8 at 25°C. Since alumina is an insoluble oxide in these environments, it may protect pure aluminum against the corrosive environment (passivity) [10].

However, aluminum and aluminum alloys are not immune to corrosion in environments containing halide ions, even at pH between 4 and 8. Environments containing chloride ions induce the local breakdown of the oxide film protecting the aluminum when polarizing the metal above a critical potential, called the pitting potential. This well known phenomenon is called pitting. Once initiated, this pitting corrosion process is autocatalytic and leads to the formation of holes (pits) on the exposed surface.

I.3.1. Factors influencing pitting initiation:

Pitting initiation is not a well understood phenomenon. Natisham et al [11] attempted to explain the process as due to the adsorption of chloride ions on to the passive film but failed to explain why chloride ions are still adsorbed on the passive film below the pitting potential. It is also proposed [12] that chloride ions interact with the passive film and generate large numbers of metal vacancies which migrate to the metal/oxide interface leading to thinning of the film by vacancy coalescence. The final breakdown would be due to tensile residual stresses. The drawback of this theory is that there is no experimental evidence of these stresses [13]. In addition, some authors have questionned the effectiveness of the protective film in aluminum alloys since experimental evidence of defects have been reported [14]. Thus, most theories are simply based on an intrinsically flawed oxide film.

In 1970, Galvele [15] proposed a model for pit initiation and pit propagation which is based only on transport phenomena. It is assumed that pitting takes place when the local pH in a surface defect reaches a critical value where the environment is able to sustain metal dissolution and prevent further repassivation. The local pH is related to the product of the current density and the defect size. Because the current density is a function of the applied potential, it is shown that pitting initiate at defects of critical size. This theory is extended [16] to account for the effect of alloy composition on the pitting susceptibility of aluminum alloys. As before, pitting initiation occurs when a driving force, as measured by the pitting potential, is large enough to sustain a proper level of metal dissolution. The rate of metal dissolution needs to be high enough to create an environment where the oxides of the alloying elements are soluble (acidic environment) and thereby prevent further repassivation.

These models of pitting initiation do not consider the role of chemical defects on the metal surface except as a source of flaws for the passive film. However, numerous experimental evidences of the role of second phase particles in pitting initiation in aluminum alloys have been reported [17, 18, 19]. These observations can be rationalized by looking at the corrosion potentials of the matrix and of the second phase particles in aluminum alloys:

Precipitates	Potential (V)	solid solution	Potential (V)
$FeAl_3$	-0.56	2024-T3	-0.69
Si	-0.26	7075-T6	-0.83
$CuAl_2$	-0.73	6151-T6	-0.83
Al_8Mg_5	-1.224	6351-T5	-0.83
$MgZn_2$	-1.05	6061-T6	-0.83
Al_6Mn	-0.85	6063-T6	-0.83

Table 4: Solution potentials of some second phase constituents measured in 53g/L NaCl plus 3g/L H_2O_2 solution versus 0.1 N Calomel Electrode [2]

Table 4 displays the potentials of some common intermetallic phases and solution-potentials of some aluminum alloys. Solution potential is essentially the potential of the matrix since the overall corrosion potential of an alloy is determined by its matrix

electrochemical behavior which constitutes the highest volume fraction [2]. As seen in table 4, the differences between the potentials of the matrix and the second phase particles are significant and will set-up galvanic cells as reported by R.Wei [20] who observed particles with a cathodic or an anodic behavior with respect to the matrix.

I.3.2. Pit growth

Pit propagation is an auto catalytic process [10, 15, 20]. Once a pit has initiated, chloride ions migrate into the pit to achieve electrical balance. Further hydrolysis of metal ions acidifies the pit environment and enhances the metal dissolution process. A cap of insoluble oxides may form at the pit mouth and impede the escape of Al^{3+} ions from the pit whereas Cl^- can still migrate inside. This greatly acidifies the pit environment and enhances the dissolution process. The cathodic reaction usually takes place on noble constituent particles for aluminum alloys or in areas away from pits. This model is primarily based on transport of ion species. However, pit propagation can also depend upon factors that are not related to transport phenomena such as grain orientation in pure aluminum. Baumgärtner, et al. [22] reported that the walls of the pits were composed of {001} facets with <001> step edges showing that some facets exhibit higher dissolution rates due to different crystallographic orientations.

I.3.3 Corrosion susceptibility of some aluminum alloy classes [3]

At this point, the phenomena of intergranular corrosion, exfoliation corrosion and stress corrosion cracking must be introduced since they share some common physical processes with the pitting process of aluminum alloys. Moreover, these material degradations are responsible for fatigue crack initiation in aircraft structures. Intergranular corrosion is a degradation process where preferential dissolution occurs at grain boundaries. Exfoliation corrosion is a form of corrosion where the attack occurs along subsurface intergranular paths parallel to the surface. Splitting of the structure is

20

observed since corrosion products have a higher volume than the initial material [2]. Stress corrosion cracking (SCC) is a synergistic process between stress and corrosion where failure occurs under a tensile load in a corrosive environment. G.H.Koch [23] has reported that a corrosive environment may promote fatigue cracking in aircraft aluminum alloys by two mechanisms of stress corrosion cracking: an anodic dissolution mechanism or by hydrogen embrittlement. Anodic dissolution is the mechanism by which cracking occurs by dissolution along grain boundaries. Hydrogen induced cracking is a process by which cracking occurs along grain boundaries that have been weakened by adsorption of atomic hydrogen.

The corrosion susceptibility of some aluminum alloy classes is presented below:

In 2xxx series aluminum alloys, $CuAl_2$ or $CuMgAl_2$ precipitates readily form along the grain boundaries, leading to a copper-depleted zone (Al-0.2% Cu) at the grain boundaries when the quenching rate is less than 1000°F/s. Thus, grain boundaries act as anodes while grain bodies and intermetallic phases $CuAl_2$ act as cathodes. It is shown by Galvele [24] that intergranular corrosion is due to a difference in pitting potentials between the different zones mentioned earlier. For 2xxx series aluminum alloys, stress corrosion cracking may occur and can be related to a preferential dissolution of some precipitates as in pitting initiation. 2024 aluminum alloy is also subject to exfoliation corrosion.

6xxx series aluminum alloys generally possess good SCC resistance. These alloys are primarily strengthened by the precipitation of Mg_2Si particles which are anodic to the matrix. Some alloys in this series can be susceptible to intergranular corrosion in the T4 and T6 temper. Pitting is the most common mode of corrosion.

7xxx series aluminum alloys can be susceptible to exfoliation corrosion or intergranular corrosion [25]. Stress Corrosion Cracking (SCC) is also a major problem in these alloys. Hydrogen embrittlement [26] has been proposed as the prevailing mechanism, of SCC though some controversy still remains.

I.4. Crack initiation

Crack initiation is dependent upon the scale of observation. In a laboratory environment, the use of replication tape allows scientists to measure cracks shorter than $10\mu m$. An optical microscope easily detect cracks of 0.1 mm length. The equipment used in the aircraft maintenance (Eddy current, ultrasonic probes) has again a different resolution. That is why crack initiation depends upon the investigator definition.

I.4.1 Factors influencing crack initiation

a) In air

Microscopic studies of fatigue crack initiation on the well known 2024 aluminum alloys [27] revealed that the cracking mode in air is dependent upon the stress level.: At high stress levels, cracking at coarse slip lines initiating in the matrix is the most likely phenomenon. At low stress levels, constituent particles appear to play a prevalent role by initiating the local coarse slip lines responsible for cracking. A.Zabett and A.Plumtree [28] also observed that most of the cracks initiate from Al_7Cu_2Fe second phase particles in 2024-T351. In the case of clad aluminum alloys, the pure aluminum layer also plays a role in crack initiation as mentioned by M.E Fine et al [29] who observed microcracking at the interface between the base metal (2024-T3 aluminum alloy) and the pure aluminum cladding. X.R Wu and J.C Newman [30] also reported that most cracks initiate in the clad layer of LC9 clad sheet in opposition with the cracking mode of 7075 bare alloy where cracks initiate at particle clusters.

b) Effect of environment

Fatigue crack initiation in corrosive aqueous environments can occur because of the stress concentration created by corrosion induced surface defects such as pits, exfoliation corrosion and intergranular corrosion. The effect of precorrosion on fatigue properties of aluminum alloys has been verified by N.L. Person [31] who reported that

fatigue cracking in smooth bending specimens occurs at pits. In addition, fatigue strengths of heavily pitted (0.2-0.3 mm) 7075-T6 and 2014-T6 bare aluminum alloys are decreased by 60% for long, 10^8 cycles, fatigue lives. The detrimental effect of intergranular corrosion is also reported for a 7075-T6 aluminum alloy lot. M.E. Fine, et al [29] also noticed that particles and pits have the same detrimental effect on fatigue crack initiation in 2024-T3 aluminum alloy. Moreover, stress corrosion cracking can also initiate defects which are detrimental to fatigue crack initiation [32]. The detrimental effect of corrosion damage on fatigue crack initiation has been reported in aircrafts [33]. S. Suresh [34] also mentioned that fatigue cracking can initiate because of an enhanced irreversibility due to the oxidation of slip steps, a preferential electrochemical attack at region of mechanically broken film and finally because of the reduction in surface energy of the alloy by adsorption of environmental species.

I.4.2 Stress concentration at the bottom of a pit

Since corrosion and fatigue processes tend to occur sequentially rather than concurrently [35], it is interesting to evaluate the stress at the bottom of a pit located on the inside of a rivet hole. Modeling a pit as an elliptical crack [36], the stress intensity factor at the tip is:

$$\Delta K = 1.12 \, \Delta\sigma \sqrt{\frac{\pi \, c \, \alpha}{Q}}$$

where $\Delta\sigma$ is the stress range, α is the aspect ratio (pit depth / pit radius) and Q is the shape factor, being equal to:

$$Q = 1 + 1.464 \, \alpha^{1.65}$$

If one considers:

- a loading of $\Delta\sigma$ = 15 ksi or 100 MPa, which is typical of the stress experienced by a fuselage skin.

- a pit of length 50 μm and aspect ratio 1, situated on the walls of a rivet hole.

Then, Q= 2.464 and α=1. $\Delta\sigma = \Delta\sigma*k_t$ where k_t is the stress concentration factor at the edge of a hole that is assumed to be located in an infinite plate:
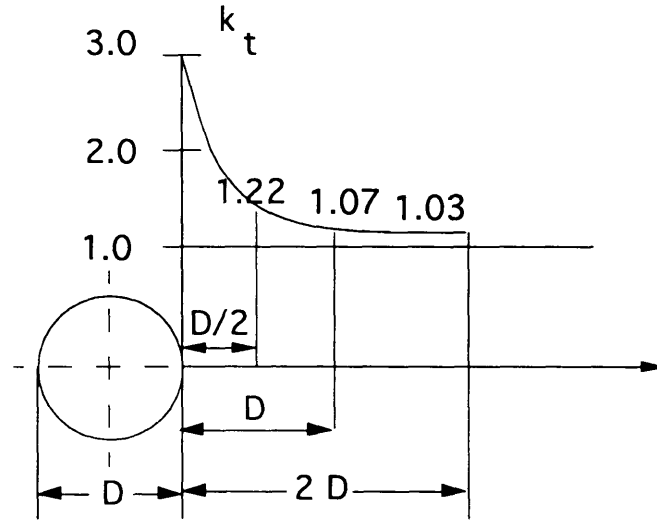
Fig.1.4: Stress distribution near a hole in an axially loaded plate [36]

From Fig.1.4, k_t can be deduced to be around 3 since 50 μm is 1/80 of the diameter. Taking k_t = 3, one finds:

$$\Delta K = 2.68 \text{ MPa}\sqrt{m}$$

This stress intensity factor is of the order of the crack propagation threshold of most aluminum alloys . Therefore a 50 μm deep pit can initiate a fatigue crack under a stress range of 100 MPa.

I.4.3 A model of fatigue crack initiation life based on pit growth

Kondo [36] has observed that the corrosion fatigue process consists of three phases: pit growth, crack formation from the pit and fatigue crack propagation. In fact, he described corrosion fatigue as a competition model between pitting corrosion and crack propagation for low alloy steel in 90°C deionized water. Measurements showed that pit radius followed a power law of exponent 1/3. Kondo assumed that transition from a pit

to a crack occurs when the fatigue crack growth rate exceeds the pit growth rate.

Modeling a pit as a elliptical crack, the equivalent stress intensity factor is given by [36]:

$$\Delta K = 1.12 \, \Delta\sigma \sqrt{\frac{\pi \, c \, \alpha}{Q}}$$

If ΔK_p is the critical experimental value for which the fatigue crack growth rate exceeds the pitting rate, one can calculate the critical pit radius at which transition from pitting to fatigue cracking takes place:

$$c_{cr} = \frac{Q}{\pi\alpha}\left[\frac{\Delta K_p}{1.12 \, \Delta\sigma}\right]^2$$
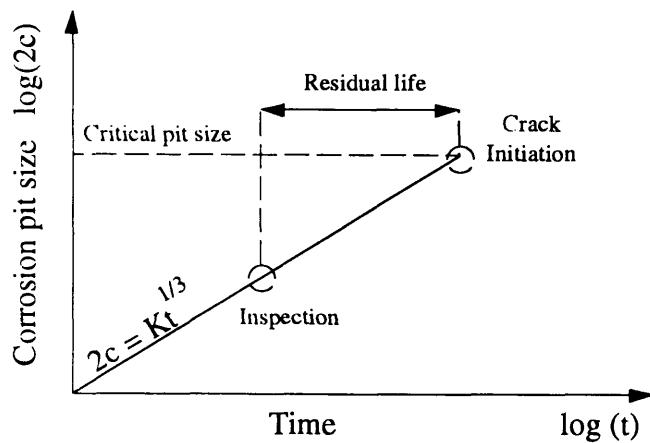
Fig.1.5: Residual life prediction of crack initiation based
on quantitative evaluation of pit[36]

Kondo's model for crack initiation life may be useful for airplane maintenance programs since it can predict the residual life before fatigue crack initiation just by measuring the amount of corrosion, as seen in Fig.1.5.

25

I.5.1 Parameters affecting fatigue crack propagation

Some parameters influencing the different regimes of crack growth are presented below:

Region I (near threshold regime): crack growth rate is very sensitive to microstructural effects, load ratio effect (R-ratio) and environmental effects. An increase in the load ratio or the presence of a corrosive environment shifts the da/dN curve up.

Region II (Paris regime): Load ratio effect and microstructural effects are low. On the contrary, some combinations of environment and frequency can be very detrimental.

Region III (fast crack propagation regime): Microstructural and load-ratio effect are very important. Environmental conditions do not play a role since the crack growth is too fast for corrosion to take place.

This rapid presentation of the problem aims at pointing out the complexity of corrosion fatigue which involves a huge number of parameters and physical processes, such as the transport of embrittling species to the crack tip, the pumping of the environment by the crack opening and closing of the crack walls, crack closure and finally fretting [34] All these physical phenomena are in turn influenced by the conditions of mechanical loading.

I.5.2 Physical and chemical processes involved in corrosion fatigue crack propagation

A corrosive environment can alter crack propagation by two different types of processes. The first one acts through purely mechanical defects. Crack propagation can be affected by pitting corrosion, exfoliation corrosion or intergranular corrosion. For instance, J.P Chubb, et al [35] studied the effect of prior exfoliation corrosion on the fatigue behavior of 7178-T6 and 2024-T351 aluminum alloys. He observed that exfoliation corrosion increases crack growth rates in 7178-T6 while no effect is apparent on 2024-T351.

A corrosive environment may also affect crack propagation through chemically induced processes. For example, hydrogen embrittlement [38] creates weak points at grain boundaries, precipitate interfaces and dislocation cores and is very detrimental when

occuring at the fracture site. This mechanism of corrosion fatigue was proposed by Smith et al [39] (cited in [23]) for 7075-T6 aluminum alloy. However, G.H. Koch [23] outlined that hydrogen embrittlement may not apply to other aluminum alloys.

Film rupture and anodic dissolution is a process by which crack advance occurs during transient anodic dissolution of metal at locations where the film has been mechanically broken [33]. Anodic dissolution and plasticity have also been associated to explain corrosion fatigue by the elimination of work-hardened metal and the stimulation of localized plastic deformation [40]. Adsorption of atoms on slip bands has been proposed to reduce the slip reversibility and enhance crack growth rates.

In reality, both chemical processes and corrosion induced mechanical defects contribute to corrosion fatigue crack propagation. In addition, corrosion may be affected by cyclic loading.

I.5.3 Models of corrosion fatigue crack propagation [34,38]

One idea developed over the last twenty years, is to consider the different combinations of crack growth rates measured under purely mechanical fatigue and versus a purely stress corrosion condition.

The models can then be divided into two categories. The first is the superposition approach where crack growth is determined by linear superposition of the crack extension rates due to the different mechanisms (purely mechanical loading, purely stress corrosion, true corrosion fatigue...). The major drawback of this model is that it does not account for the interaction between the mechanisms of crack extension. In fact, the proposed mechanisms probably do not form an orthogonal basis. However, it can be used to explain the observed shape of the da/dN curve. Some weights can be used in the linear superposition to adjust the shape. However, these weights are empirical and cannot be determined from microstructural variables or the environmental composition.

27

The second category is to consider that the proposed mechanisms are mutually competitive and that the crack growth rate is determined by the fastest mechanism available. Again, the synergistic effect are difficult to incorporate into the model.

In addition, some attempts have been made to develop models based on crack-tip mechanics rather than on stress intensity factor only. Some authors have also taken interest in developing models for the occluded crack chemistry which is undoubtedly different from the bulk and consequently plays a prevailing role in fatigue corrosion crack growth [38].

As a conclusion, most of the life prediction models rely heavily on empirical data (da/dN curves) that are used to integrate the fatigue life from an initial crack size to the final crack size [41].

II. Microstructural Characterization of 6013-T6 alclad aluminum alloy

The as-received material is a 6013-T6 alclad sheet supplied by Alcoa. Its dimensions are 48"x60"x0.045". The average micro hardness is 133.5 HV.

II.1 Second phase particles

Cross-sections were cut parallel to the three principal planes, T-S, L-S and L-T, where L is the rolling direction, S the sheet thickness and T the transverse direction, perpendicular to S and L. Samples were mounted and polished down to 0.05 μm with alumina slurries. They were then examined unetched with an optical microscope. A cross-section of the base metal is displayed in Fig.2.1. Constituent particles and dispersoids can be observed. Constituent particles appear light gray. Some are script like. Others are elongated in the rolling direction. Some are broken or form clusters. The volume fraction of the constituent particles is measured using two methods: the point count and an image processing technique. The point count method gives a volume fraction of 1.62±0.1% with 95 % confidence limits as determined using the Dehoff method[42]. It is measured using a 10x10 grid placed at random location 5 times on each of the 8 micrographs under consideration.

T-S plane	L-S plane	L-T plane
1.05%	1.06%	0.86%
1.2%	1.25%	1.42%
1.305%	1.51%	1.936%
0.95%	0.76%	0.65%
-	0.39%	0.94%
1.13 %	1.0%	1.16%

Table 5: Volume fraction of the constituent particles as calculated with an image processing technique.

The image processing technique calculates a volume fraction of 1.1 %. The surface fractions are calculated on three different planes. Table 5 displays the results. It must be noted that these last values underestimate the real volume fraction since some

Fig.2.1: 6013-T6 aluminum alloy. Unetched (x1000).
Gray constituent particles and fine dispersoids can be seen
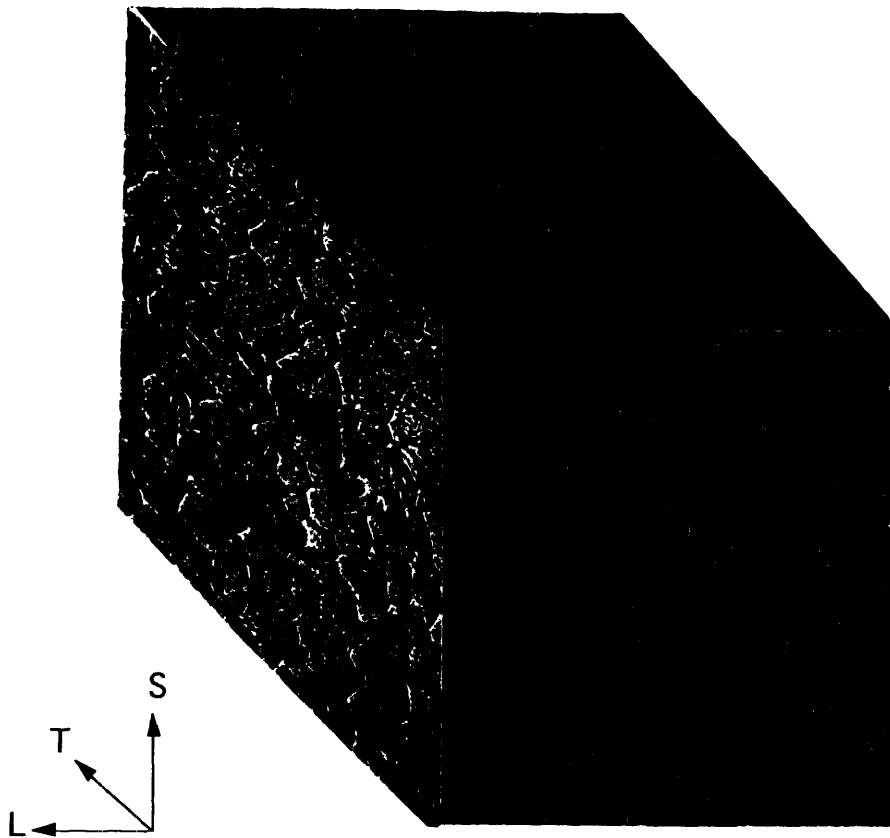
Fig.2.2: 6013-T6 aluminum alloy sheet. Etched with Keller's reagent (x200)

procedures of the image processing erode or erase particles. Particle densities are displayed in table 6:

T-S plane	L-S plane	L-T plane
73646 part/cm^{-2}	79537 part/cm^{-2}	58916 part/cm^{-2}
79537 part/cm^{-2}	85429 part/cm^{-2}	50079 part/cm^{-2}
70700 part/cm^{-2}	100158 part/cm^{-2}	76591 part/cm^{-2}
85429 part/cm^{-2}	58916 part/cm^{-2}	47133 part/cm^{-2}
61862 part/cm^{-2}	41242 part/cm^{-2}	61862 part/cm^{-2}
74234 part/cm^{-2}	73056 part/cm^{-2}	71289 part/cm^{-2}

Table 6: 6013-T6: Particle density

EDAX analysis of the constituent particles shows a content of aluminum, silicon, manganese, copper and iron. Magnesium is not detected. The results are displayed in tables 7, 8 and 9. According to [2], they may be $(Fe, Mn)_3Si_2Al_{12}$ type particles. Indeed, for these three particles, table 10 shows some ratios which are in accordance with the chemical composition of $(Fe, Mn)_3Si_2Al_{12}$ particles.

Particle number	1	2	3	Theoretical
Al/(Si+Cu)	8.1	6.5	5.9	6
Al/(Fe+Mn)	3.81	3.8	4.01	4
(Fe+Mn)/(Si+Cu)	2.1	1.71	1.47	1.5

Table 10: Ratios of the different amount of elements (expressed in atom percent)

The difference between the experimental and theoretical values can be explained by two factors. The first is due to the x-ray beam that may analyze some of the surrounding matrix when the particles are too small. The second factor is due to the mix of intermetallics such as $(Fe, Mn)_3Si_2Al_{12}$ and $(Fe, Mn)_3SiAl_{12}$.

31
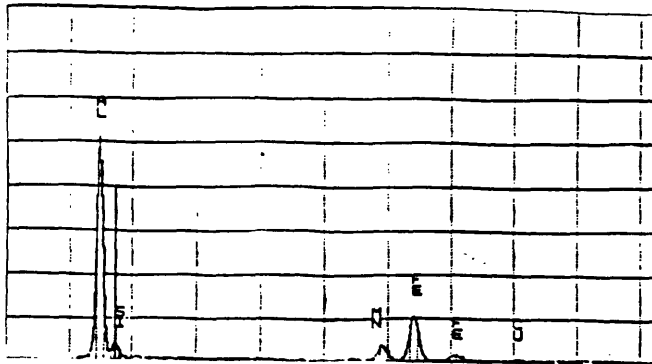
Aluminum (Al)	Iron (Fe)	Manganese(Mn)	Silicon (Si)	Copper (Cu)
72.28 at%	14.68 at%	4.28 at%	7.28 at%	1.64 at%

Table 7: Chemical composition of particle 1 and EDAX spectrum
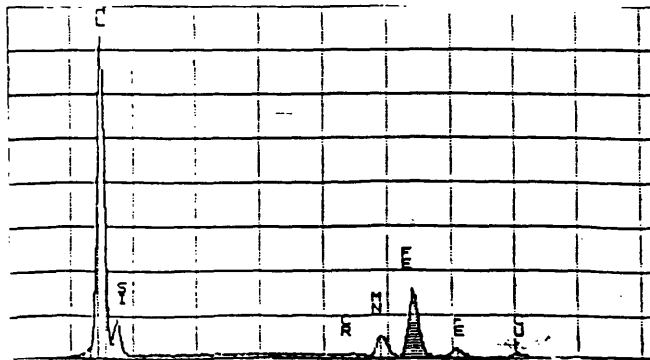
Aluminum (Al)	Iron (Fe)	Manganese(Mn)	Silicon (Si)	Copper (Cu)
69.96 at%	14.22 at%	4.17 at%	8.88 at%	1.87 at%

Table 8: Chemical composition of particle 2 and EDAX spectrum
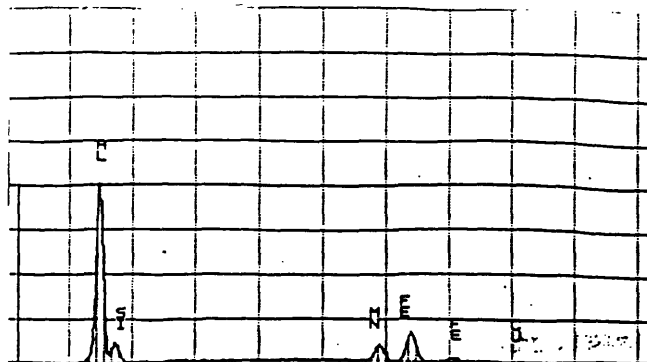
Aluminum (Al)	Iron (Fe)	Manganese(Mn)	Silicon (Si)	Copper (Cu)
69.32 at%	11.59 at%	5.67 at%	10.04 at%	1.69 at%

Table 9: Chemical composition of particle 3 and EDAX spectrum

Fig.2.3: Optical micrograph of a 6013-T6 alclad aluminum alloy sheet cross-section.

Etched with Keller's reagent.(x330)
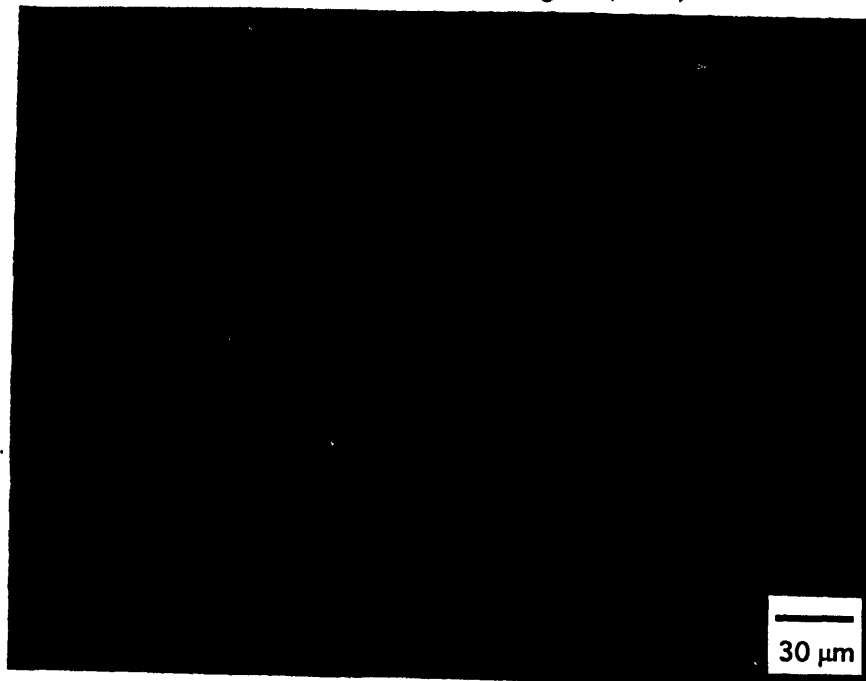
Fig.2.4: Optical micrograph of a 2024-T3 alclad aluminum alloy sheet cross-section
Etched for 3 minutes in an aqueous solution containing 2g NaOH and 5g NaF (x330)

The dispersoids and precipitates are probably Mg_2Si, $Cu_2Mg_8Si_6Al_5$ and $CuMgAl_2$ as seen in chapter I. No EDAX analysis was carried out because of the dimensions.

II.2 Grain Size

Grain size is recorded by metallographic examination of 6013-T6 alclad sheet sections in T-S, L-T and L-S planes. Specimens are mounted and mechanically polished with silicon carbide paper down to 5 μm. Afterwards, 1, 0.3 and 0.05 μm grades alumina slurries are used. After ultrasonic cleaning, the sections are etched with Keller's reagent by swabbing for two minutes. Micrographs of the sections are taken at random location on two samples. Grain size was measured using the linear intercept method. This gives to an average grain size of 19 x 25 μm on both L-S and T-S planes, the grains being slightly elongated in the rolling direction. Grains in the L-T planes are slightly larger indicating that the overall grain shape was flattened in the rolling plane as expected. As a comparison, 2024-T3 grains are significantly elongated with a dimension of 60x25 μm. This probably accounts for a better performance of 6013-T6 in stretch-forming operations as reported in [7] and [8]. A perspective view of aluminum alloy 6013-T6 sheet can be seen in figure 2. Fig.2.3-2.4 show the difference between the grain texture of 2024-T3 and 6013-T6 aluminum alloys.

II.3 Cladding

Samples of the sheet are cut along the T-S and L-S plane, mounted and polished down to 0.05 μm with alumina slurries. After ultrasonic cleaning, samples are etched with Keller's reagent by swabbing for two minutes. Cross-sections are examined with an optical microscope. The base metal is etched and the cladding did not exhibit any form of attack. Then, the cladding thickness is calculated by measuring the unattacked part of the sample. The cladding thickness is 60-70 μm on each side. This represents roughly 10 % of the total thickness which is 0.045 inches or 1.143 mm.

III. 6013-T6 alclad and 2024-T3 alclad : corrosion performances in ASTM G69

III.1. Experimental Procedures

III.1.1 Solution-potential (ASTM G69)

Samples are cut parallel to the L-T plane. On one side, a nickel wire is pasted with silver paint for electrical contact. When the silver paint is dry, the contact is covered with glue. Then, the assembly was cold mounted. The side opposite to the wire is directed outward. After curing, grinding is used to remove the aluminum cladding. The sample is polished down to 0.05 μm with alumina slurries and cleaned in an ultrasonic bath. Afterwards, a lacquer is applied around the specimen to seal and prevent crevice.

The solution-potential of 6013-T6 aluminum alloy is measured using ASTM G69 [43]. One liter of ASTM G69 consists of 58.5±0.1g of NaCl and 9±1mL of H_2O_2 at 30%.

III.1.2 Corrosion tests

a) Samples Preparation

In this study, samples are cut from either from 6013-T6 or 2024-T3 alclad aluminum alloy sheets. Their dimensions are 1x1 cm. They are cold mounted in order to polish one side to 0.05 μm grade with alumina slurries. They are cleaned in an ultrasonic bath for 15 minutes to remove any particle that might have been embedded in the matrix during the polishing stage. After, the samples are taken out of the bakelite and cleaned in acetone.

b) Experimental Set-Up

After preparation, the specimens are immersed in a beaker containing 2 liters of ASTM G69. Samples are held with a plastic mounting clip. The surface under study is facing upwards. During the whole experiment, a pump aerates the solution. The solution is changed every 2 hours for the first 12 hours to keep the hydrogen peroxide level high.

The solution pH is measured before and after changing. The experiments are carried out at room temperature.

III.2. Results

III.2.1 Solution-potential

The measured solution-potential is -741 mV versus a Saturated Calomel Electrode (SCE) at 25°C. 92 mV must be subtracted from the previous value to convert to the standard of 53g/L of NaCl with 9 mL of H_2O_2 , measured against a 0.1 N calomel electrode [43]. This gives -833 mV, which is in good agreement with the literature, which gives a value of -830 mV for the 6xxx series in the T6 temper [2].

III.2.2 Pit Morphology

Two types of pits are observed. The first consists of large pits (Fig.3.2-3.4). The latter are roughly hemispherical, at least before they coalesce with neighboring pits. Low magnification micrographs clearly show that pits initiate around constituent particles (Fig.3.2-3.3) at short times. In addition, particle density correlates well with the density of these large pits, after 30 minutes immersion in ASTM G69, as seen in the table:

Density: number/cm^{-2}	Pits	Particles
	52690	73646
	72594	79537
	59715	70700
	54797	85429
		61862
		79537
		85429
		100158
		58916
		41242
Average	60886	73646
Standard Deviation	8389	16548

Table 11: Particles and large pit density in 6013-T6 aluminum alloy.

Since these particles appear to be unaffected by the solution, it can be assumed that they are cathodic to the matrix. At longer immersion times, constituent particles cannot be seen except in some pits where the pit cavity has reached a second layer of constituent particles. The shallow shape of the pits may be explained by the small potential difference between the constituent particles and the matrix.

High magnification micrographs show some pits in the order $1\mu m$. These are probably due to dispersoids. There is a preferential pitting along grain boundaries which leads to an intergranular type damage as seen after 6 hours. The edges are clearly defined and the surrounding matrix is not attacked (Fig.3.6). No particle is detected. This proves that this pitting process is due to precipitates which are anodic to the matrix (if due to precipitates). In this case, the particles that can be involved are either Mg_2Si or excess Si, since their open circuit potential is less noble than pure aluminum (6xxx series). One must mention some dark spots in Fig.3.4. These are probably not yet growing pits: some dissolution takes place and darkens the surroundings of some precipitates. For the first six hours, the overall pit density increases linearly with time as shown in Fig.3.7. After, it is difficult to define a pit density, since some localized intergranular corrosion occurs as mentioned earlier. In addition, evidence of this intergranular corrosion is given by examination of the cross-sections, where a very narrow intergranular corrosion is detected (Fig.3.8). At the transition cladding/base metal, no specific form of corrosion is reported.

Metallographic cross-sections show that the pit density is lower in 2024-T3 alclad than in 6013-T6 alclad. Pits are narrow and deep. Some intergranular corrosion is associated very often with the deepest pits (Fig.3.9-3.10)

Fig.3.1: Optical micrograph of 6013-T6 aluminum alloy. As received, unetched (x300)
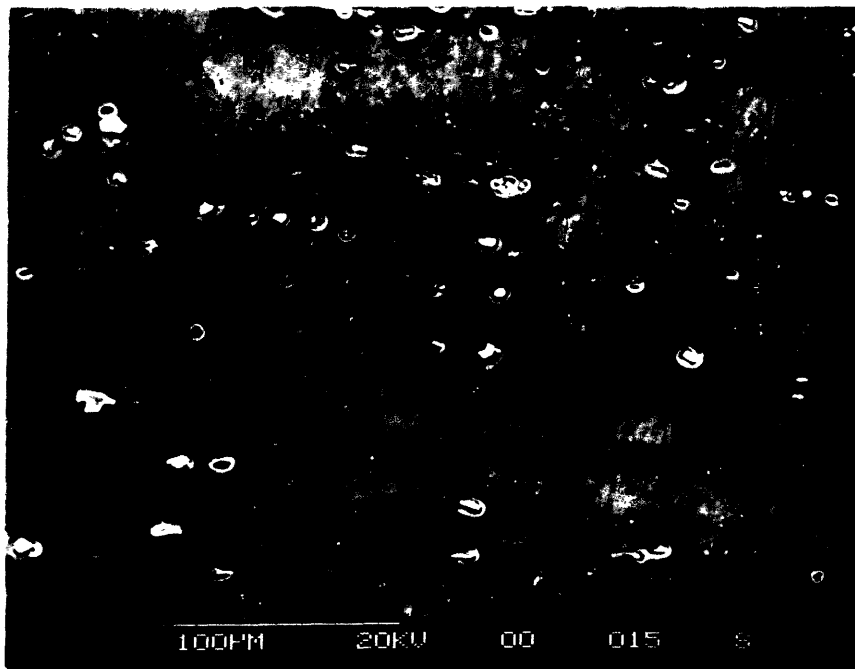
Fig.3.2: SEM micrograph of 6013-T6 aluminum alloy. 30 minutes in ASTM G69 (x300)

38
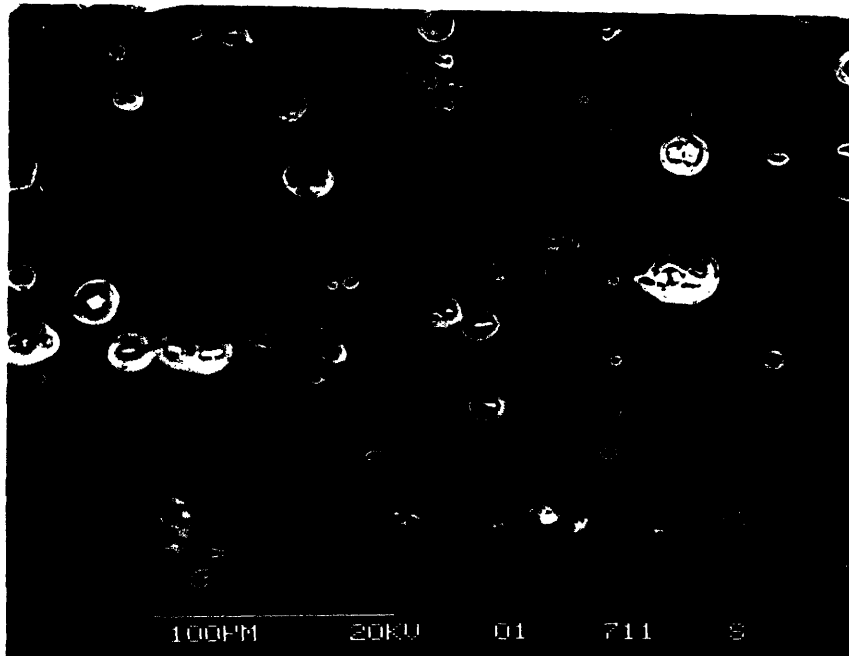
Fig.3.3: SEM micrograph of 6013-T6 aluminum alloy. 1 hour in ASTM G69 (x300)
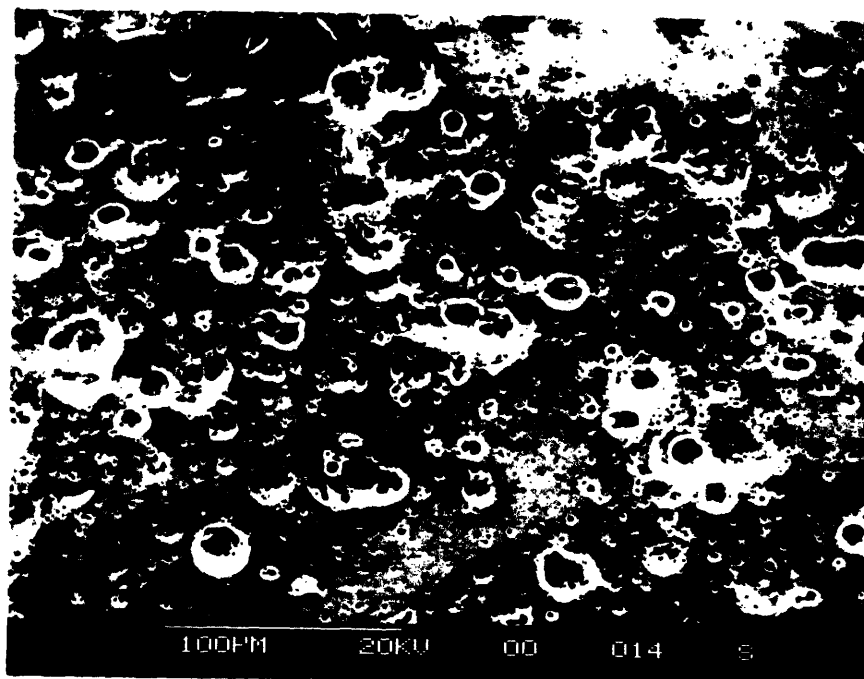
Fig.3.4: SEM micrograph of 6013-T6 aluminum alloy. 6 hours in ASTM G69 (x300)
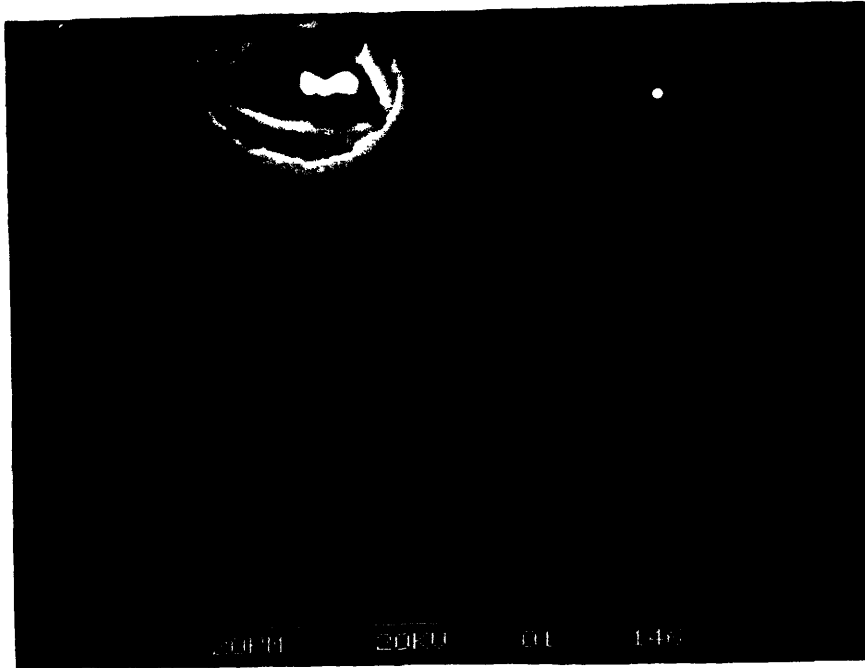
Fig.3.5: SEM micrograph of 6013-T6 aluminum alloy. 1 hour in ASTM G69 (x1710)

Fig.3.6: SEM micrograph of 6013-T6 aluminum alloy. 6 hours in ASTM G69 (x1710)
Some pitting at the grain boundaries can be observed.

III.2.3 Pit depth

Pit depth is recorded through metallographic examination. The samples are cross sectioned at random locations and polished. The pit depth was taken as the measured value on the cross-section. It must be noted that this measurement cannot represent the true pit depth since a pit is a three dimensionnal defect and a random cross section does not intersect the bottom of each pit. However, since the maximum pit depth is the point of interest, 10 samples were examined for each immersion time and the maximum depths recorded. In Fig.3.11-3.12, pit depth frequency is displayed. It can be seen that the distribution extends to the deep pits at large times, as expected.

On the graph showing the maximum pit depth (Fig.3.13), each point represent the maximum pit depth recorded for one set of samples tested together in the same solution. The data shows some scatter that can be due to:

- Measurement accuracy since the cross-sections may not intersect the maximum depth of the deepest pits.

- Environment fluctuations such as temperature and solution composition. ASTM G69 solution is difficult to control because of the hydrogen peroxide which decays upon standing. In addition, the ASTM specifications are 9±1 mL which may not be accurate enough.

However, the time dependence for 6013-T6 aluminum alloy is found to be a power law of exponent 0.37 which is not irrelevant when compared with the corrosion data found in the literature which reports an exponent of 0.33 [43].

For 6013-T6 alclad, no significant difference in maximum pitting depth on the different orientations was recorded. This can be explained by the equiaxed structure of the grains.

41

6013 T6 in ASTM G69
Overall pit density as a function of time

$$y = -1.2323e+05 + 6.6964e+05t \quad (R= 0.99236)$$

Pit Density (number of pits/cm^2)

Time (hours)
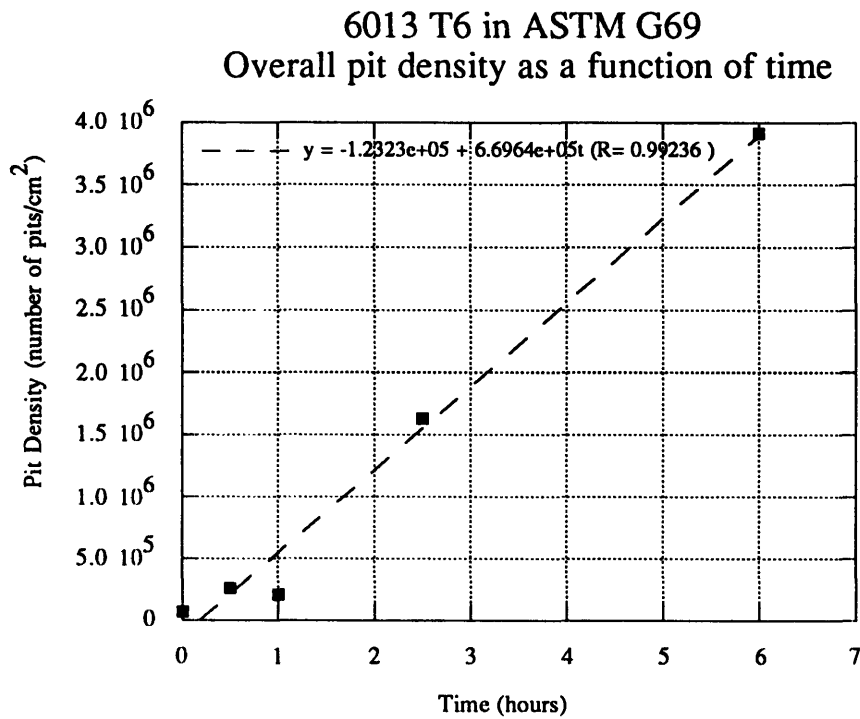
Fig.3.7: Overall pit density for 6013-T6 aluminum alloy immersed in ASTM G69
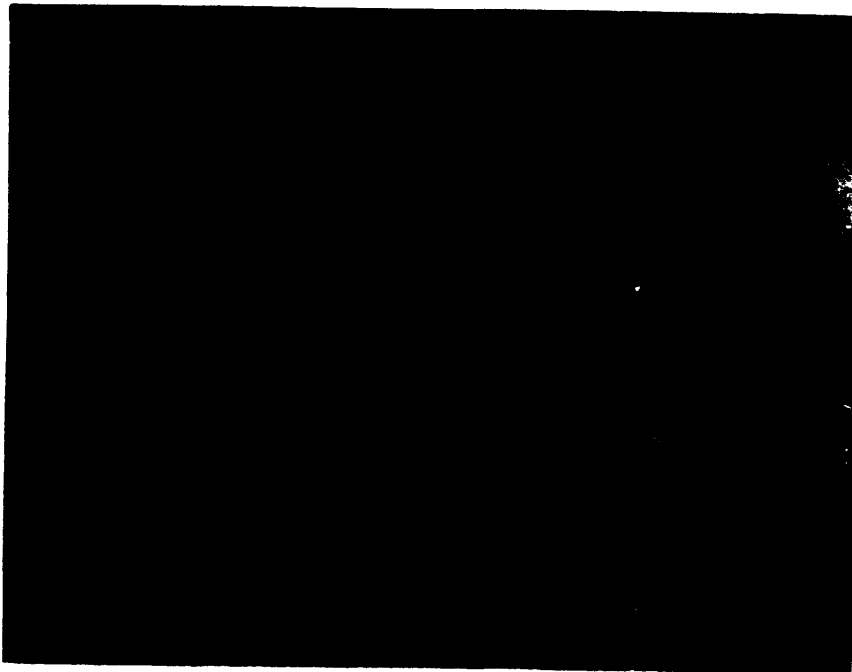
Fig.3.8: 6013-T6 alclad aluminum alloy sheet cross-section. The specimen was scratched prior to a 60 hour immersion in ASTM G69. Intergranular corrosion follows a very narrow path. (x1000)

42
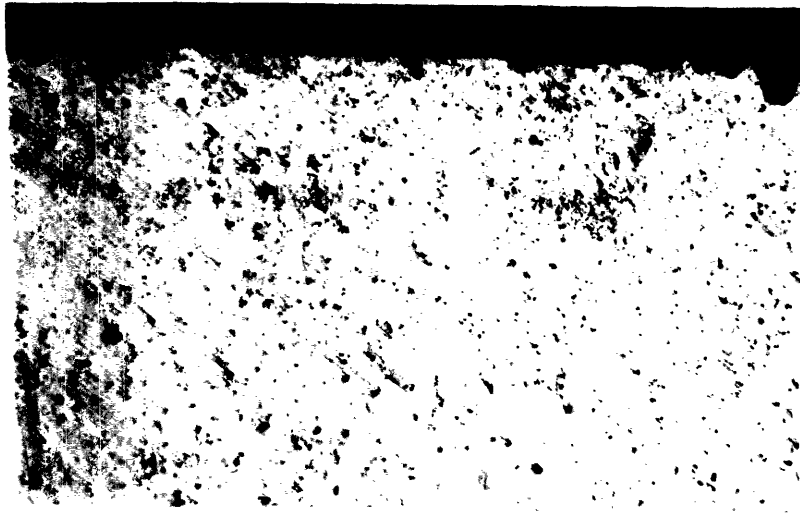
Fig.3.9: Optical micrograph of 6013-T6 alclad aluminum alloy. Cross-section of the T-S plane. Corroded 6 hours in ASTM G69 (x200)
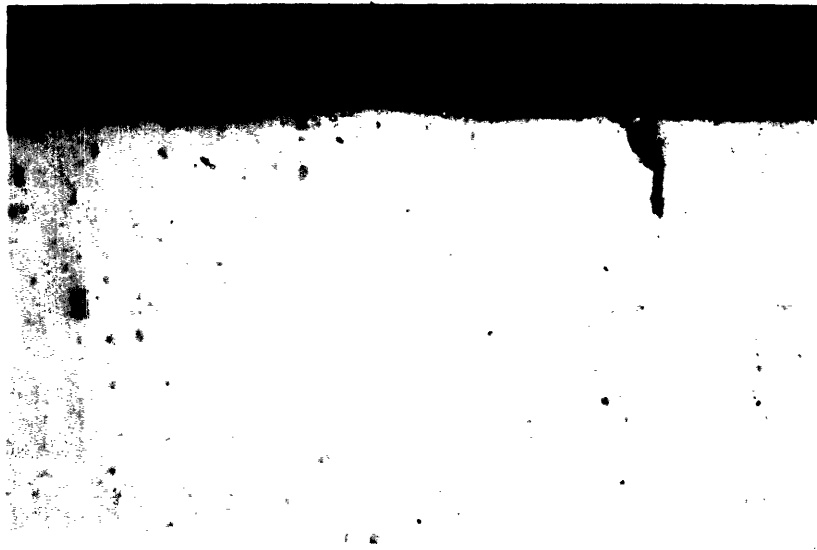
Fig.3.10: Optical micrograph of 2024-T3 alclad aluminum alloy. Cross-section of the T-S plane. corroded 6 hours in ASTM G69 (x200)
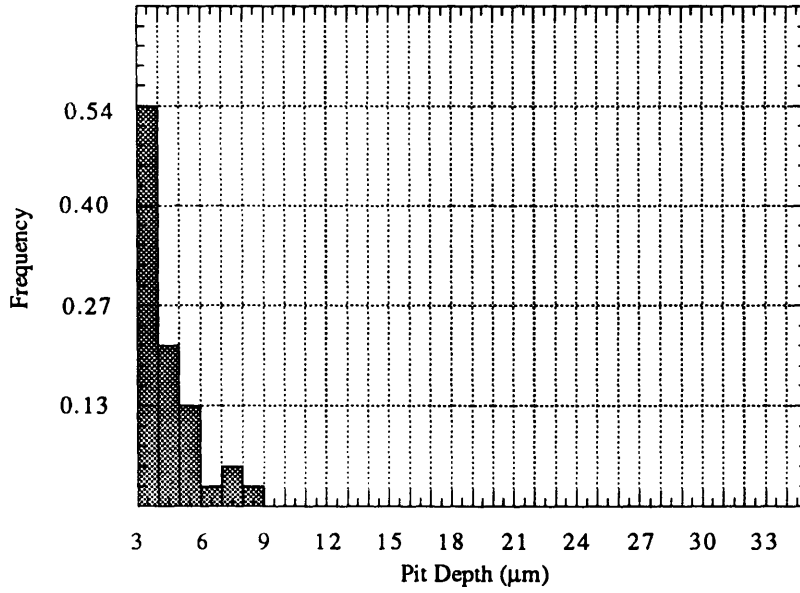
Fig.3.11: 6013-T6 alclad: Pit depth frequency after one hour immersion in ASTM G69
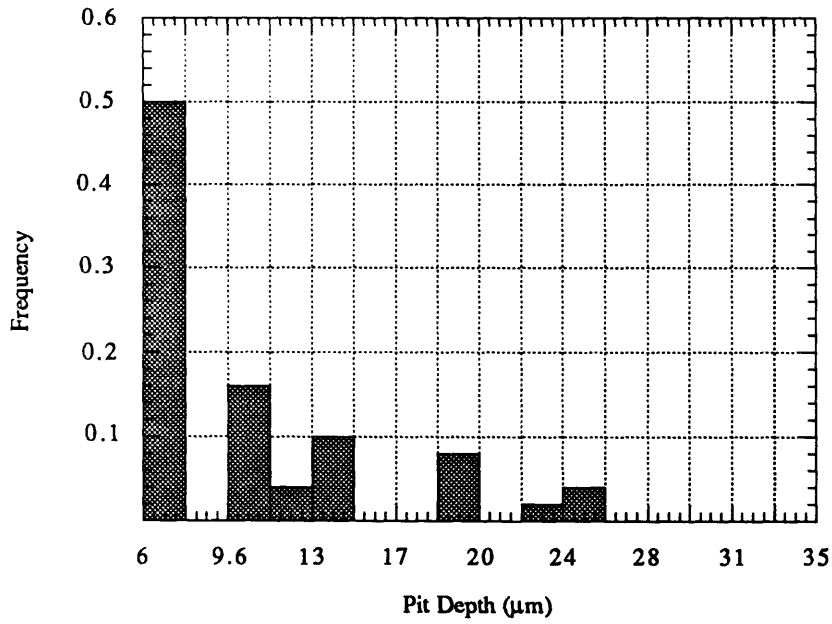
Fig.3.12: 6013-T6 alclad: Pit depth frequency after six hour immersion in ASTM G69

44
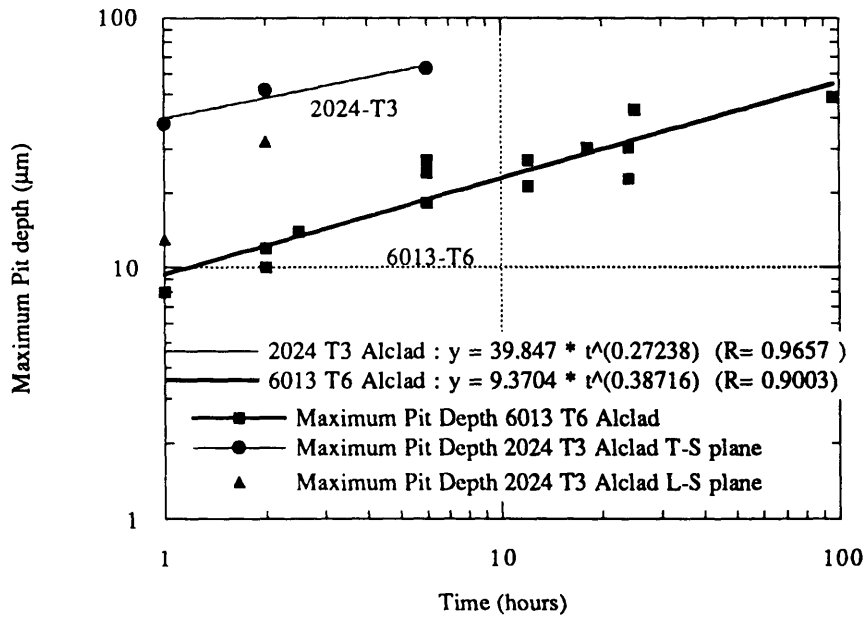
Fig.3.13: Maximum pit depth as a function of immersion time in ASTM G69 solution
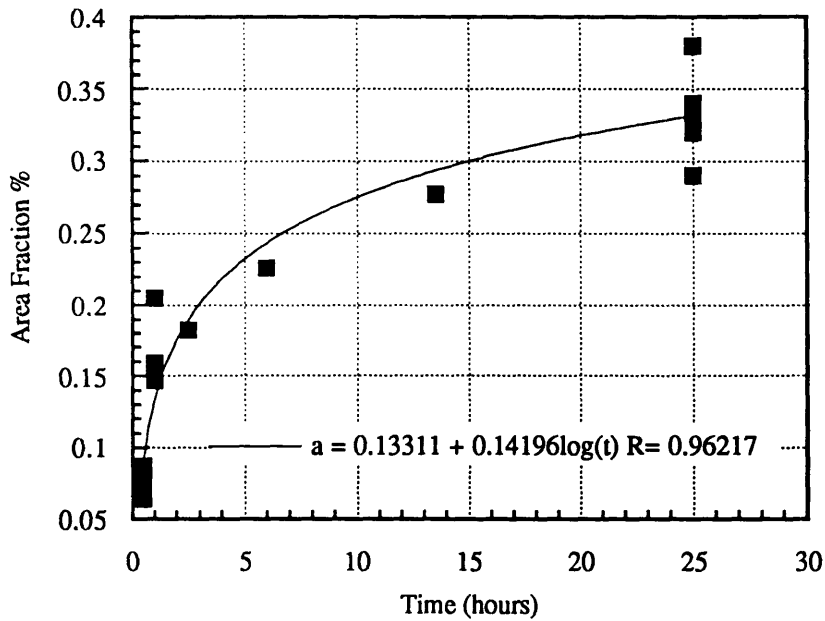
Fig.3.14: 6013-T6 alclad: Pit area fraction on T-S and L-S plane as a function of the immersion time in ASTM G69 solution.

45

For 2024-T3 alclad, a significant difference is observed between the T-S plane and the L-S plane, the T-S plane being the worse. Since pitting is associated with some intergranular corrosion, the preferential pitting on the T-S plane may be explained by a higher number of grain boundaries in the T-S plane.

III.2.4 Pit Area Fraction

Pit Area Fraction exhibits a logarithmic dependence with time (Fig.3.14). An attempt to correlate the pit area fraction with a power law gives an exponent of 0.37 but the correlation is unsatisfactory. In fact, the pit area fraction is mostly due to the large pits seen in Fig.3.2-3.4. These do not grow laterally too much as seen on the pit area distributions of Fig.3.15-3.16. Some Pits grow by coalescence rather than by a true lateral growth. The cathodic protection provided by the cladding may explain this logarithmic dependence.

III.2.5 Aluminum cladding:

An EDAX analysis shows that the cladding is pure aluminum. However, pits develop in a clear crystallographic manner as in pure aluminum (Fig.3-18). Bands of shallow square pits oriented along the rolling direction are observed (Fig.3-17). In the cross-sections, pits are observed on the whole thickness. Pitting kinetics is difficult to establish due to a surface processing problem. In fact, one side of the cladding is preferentially corroded. After eliminating the experimental bias, the cladding is slightly polished on both sides and the sample is immersed again in ASTM G69. In this case no selective attack is found. The cladding thickness is measured after polishing and gives a thickness of 48-60 μm to compare with an initial thickness of 60-70 μm, demonstrating that the cladding remains after polishing.
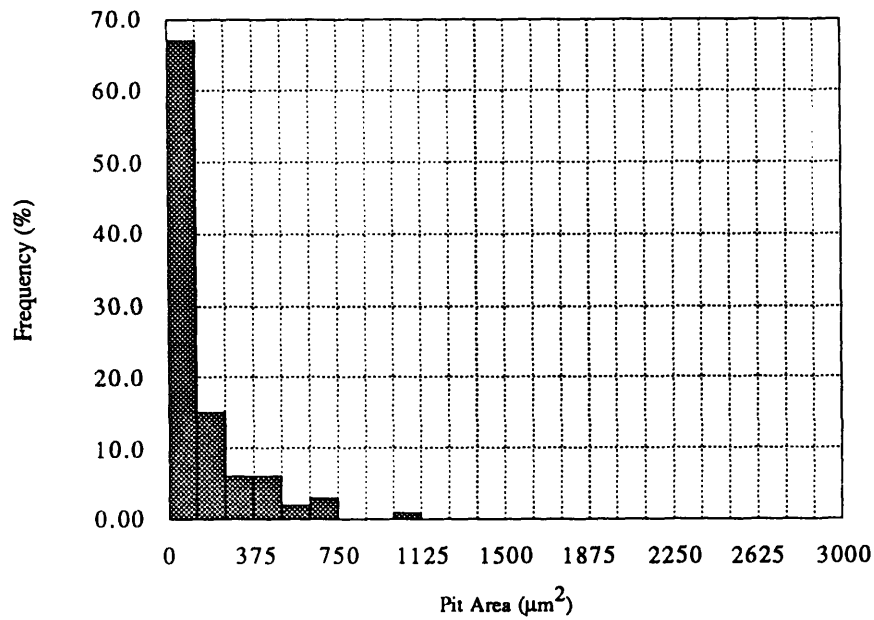
Fig.3.15: 6013-T6: Pit area distribution after one hour immersion in ASTM G69.
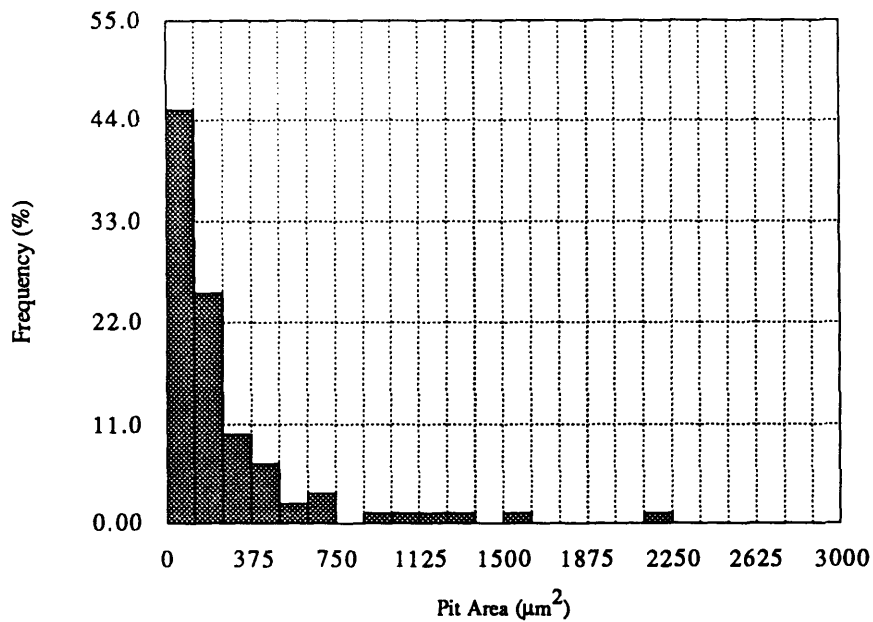
Fig.3.16: 6013-T6: Pit area distribution after six hour immersion in ASTM G69.

47
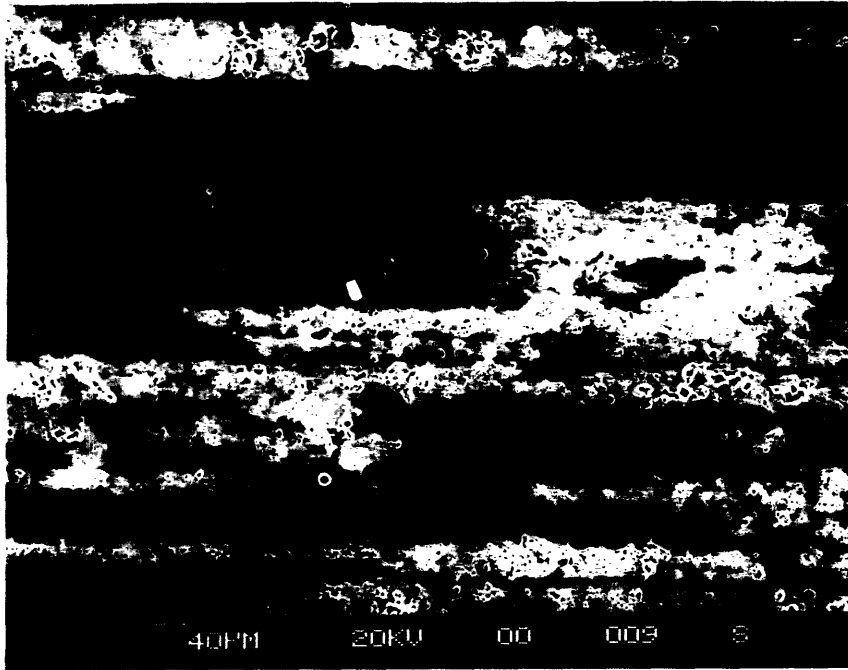
Fig.3.17: 6013-T6 alclad aluminum: Cladding after 12 hour immersion in ASTM G69 Crystallographic pitting has occured along the rolling direction (x70)
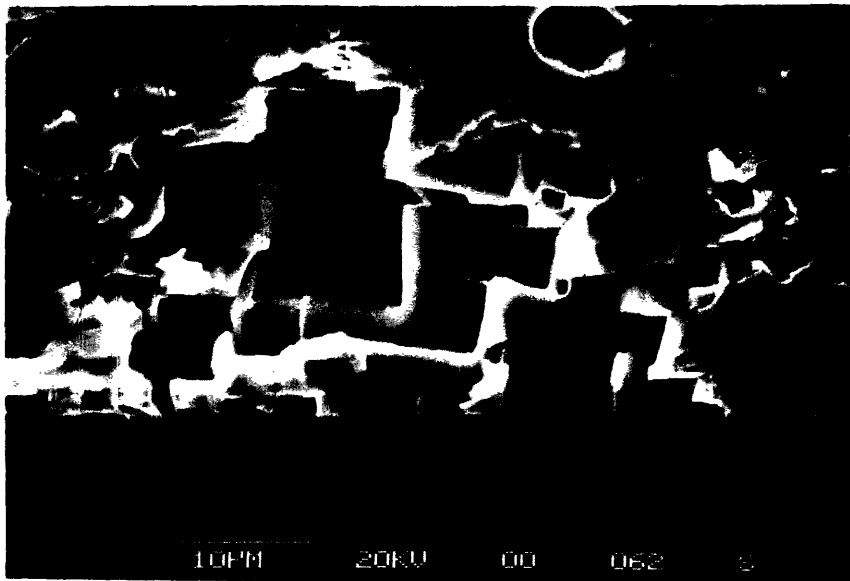
Fig.3.18: 6013-T6 alclad: Cross-section corroded for 6 hours in ASTM G69. Pitting in the cladding is clearly crystallographic (x1800)

To measure pit depth, the samples are cross-sectioned perpendicular to the rolling direction since the pits are along this direction. Table 12 displays the results:

Immersion times	6 hours	12 hours	18 hours	24 hours
Pit Depth (μm)	15.1	21.2	18.1	18.1
	18.1	21.2	24.24	15.1
	9	21.2	21.2	18.1
	19.7	15.1	27.2	22.7
	6.1		12.1	33
			15.1	27.2
			18.1	6
			18.1	3
			21.2	4.54
			30.3	24.2
			18.1	24.2
				12.1
				35
Mean	13.6	19.67	20.34	18.7
Maximum	19.7	21.2	30.3	35

Table 12: 6013-T6: Pitting depth recorded on one side of the cladding

On the contrary, observation of electrochemical behavior of 2024-T3 alclad aluminum alloy is quite different. General dissolution of the cladding is seen as expected in this kind of material. However, cross-sections of the base metal show some pits which are usually associated with exfoliation type corrosion and precipitates. They are very rare but deeper than in the case of 6013-T6 alclad. Comparison with unclad material clearly show the effect of the cladding on the pitting behavior. In unclad 2024-T3, pits are more numerous, bigger and broader.

IV.1. Experimental procedures for corrosion fatigue experiments

IV.1.1 Sample geometries

All specimens are machined from as received 6013-T6 alclad sheet in the TL orientation: the tension axis is perpendicular to the rolling direction and is in the plane of rolling. This is the orientation of aluminum sheets used in the aircraft industry. specimen geometry is based on a rectangle of dimensions 6x3x0.045 inches. At each end, grip attachment is provided by a row of 1/4 inch diameter through-holes.

a) Specimens designed for the study of crack initiation

The specimen geometry is displayed in Fig.4.1. Centered holes with and without countersink are investigated. Their diameter is 0.159 inches or 4.03 mm, which is standard for a aircraft rivet hole. The hole cross-sections are displayed in Fig.4.2. A smaller gage width is machined in order to insure crack initiation at center holes thus preventing failure at the grip holes.

Countersunk hole (mm)

Straight shank hole (mm)
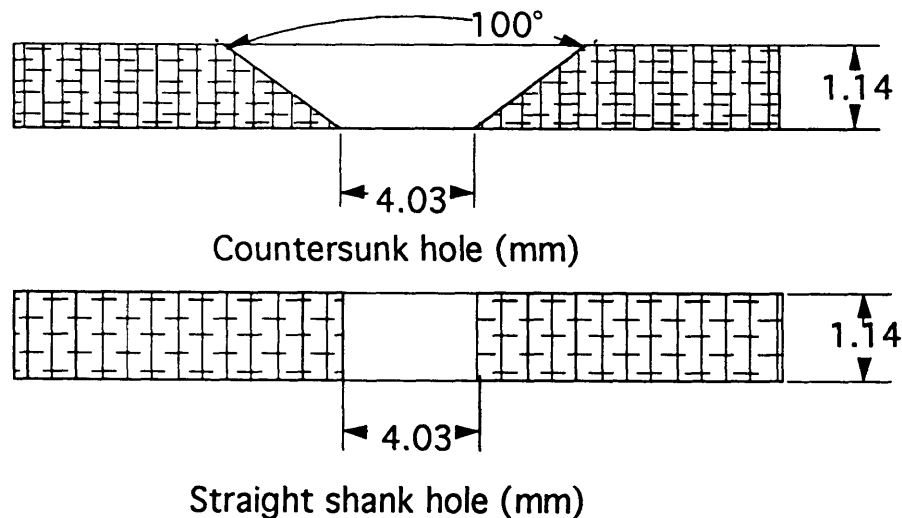
Fig.4.2: Hole geometries of specimens designed for the study of crack initiation.

The walls of the center hole are polished mirror-like with diamond paste (1μm grade). This procedure insures against surface defects from machining which could interfere

with the study of the surface condition effect. Also, the surface around the hole is polished to detect the early stages of crack initiation. However, it is almost impossible to remove the machining marks on the countersunk.

b) Specimens designed for the study of crack propagation

The samples are machined on the base of Center Cracked Tension specimens (CCT). At the center of the plate, the 1/8 inch hole is extended by two sawcut (jeweler saw) notches on both sides, such that the total notch is perpendicular to the tensile axis and is about 0.5 inches long. Its width is around 0.03 inches. This facilitates crack initiation. The geometry is shown in Fig.4.3.

IV.1.2. Experimental set-up

a) Crack initiation

A model 1331 Instron is used to perform the fatigue test using a sine wave form. The tests are carried out at 10 Hz. An R-ratio of 0.05 is chosen since it represents the real load ratio undergone by aircraft fuselage skins. Stress ranges of 100, 120, 140 MPa are used for countersunk hole specimens and 100, 120, 140, 170 and 220 MPa for open straight hole specimens.

Crack initiation is defined as the number of cycles necessary to grow a crack of a given length (0.4 mm for chamfer hole and 0.5 mm for straight hole). Crack initiation is monitored with a travelling microscope (Fig.4.4) on one side of the sheet and a magnifying glass on the other side.

b) Crack propagation

As for crack initiation, an Instron 1331 is used for fatigue testing. The experiments are run with a sine wave and a frequency of 10 or 0.1 Hz.

Two R-ratios are applied, namely 0.05 and 0.33. As mentioned earlier, 0.05 is the load ratio experimented in service flight by fuselage skins. 0.33 is chosen to investigate the influence of an overload on crack growth rates. At R=0.05, the minimum and maximum loads are respectively 0.035 KIP and 0.7 KIP. At R=0.33, the minimum and maximum loads are respectively 0.333 and 1 KIP. With an average cross-section of 0.13 inches, the equivalent stresses were 1.72-34.5 MPa for R=0.05 and 16-48.5 MPa for R=0.33.

Once a crack is initiated, the crack length is measured using a traveling microscope without stopping the test. The measurement is done periodically by moving the microscope from one crack tip to the other. At high crack growth rates, the test is stopped during the measurement for accuracy.

c) Tests run in solution

Some tests are run in ASTM G69 to evaluate the effect of active corrosion on both crack initiation and crack propagation. A clear plastic chamber with an open top and slot at the bottom is attached to the specimen using silicon rubber cement. Crack initiation and propagation are monitored as above. Fig.4.5 displays the set-up.
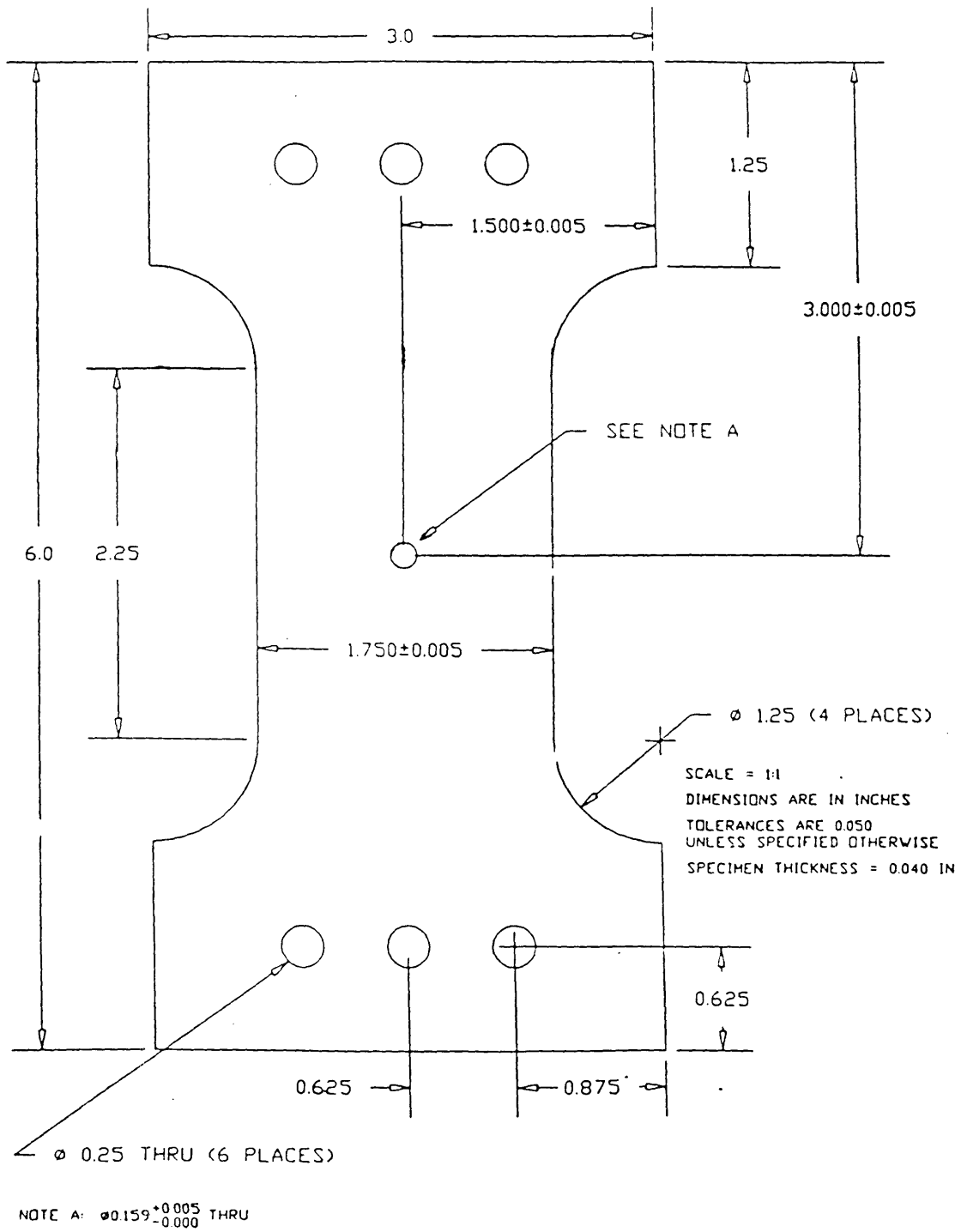
Fig.4.1: Specimens designed for crack initiation

30

1.5

0.5

30

6.0

ø 0.125 THRU

SCALE = 1:1
DIMENSIONS ARE IN INCHES
TOLERANCES ARE 0.050
UNLESS SPECIFIED OTHERWISE
SPECIMEN THICKNESS = 0.040 IN

0.625

0.625   0.875

ø 0.25 THRU (6 PLACES)

Fig.4.3 CCT specimens

54

Load Cell

Measurement Dial

Grips

Specimen

Position Adjust
Dial

Eye Piece

Strobe Intake

Travelling
Microscope
Frame

(Attached to Load
Frame)

Grips

Actuator

Scale = Approx. 1.4

Fig.4.4: Experimental set-up

GRIP HOLES

CLEAR PLASTIC BOX
(OPEN TOP)
0.125 THICK WALLS

2.5

NOTCH

4 0

1.0

3 1/16 × 1/16 SLOT
THRU - SEALED
..@ BOTTOM CENTER

CCT SPECIMEN

DIMENSIONS ARE IN INCHES
SCALE: APPROX. 1:1

Fig.4.5: Set-up for tests run in ASTM G69

56

V. Experimental results of corrosion fatigue experiments

V.1. Crack initiation

Because of the cladding softness, extensive deformation takes place around the hole causing difficulty in detecting the main crack when its length was less than 0.4-0.5 mm. In fact, the cladding is covered by lines which appeared black under the strobe light and can be mistaken as cracks (Fig.5.1-5.2). Moreover, some cracks initiate around the hole and stop propagating: since crack initiation is defined as the length of the crack which will lead to complete fracture, some intrinsic uncertainties remain.

In addition, it is difficult to detect cracking with the magnifying glass. For a chamfer hole, this is not a problem since fatigue cracking always initiates at the countersink (the crack is seen propagating along the countersink after initiation on the other side for all cases).

Results are displayed in Appendix 1. For the chamfer hole case, accuracy in the number of cycles is evaluated to 1,000 cycles. This represents 3% of the initiation life. The effect on the propagation life is worse since it can reach 10%.

IV.1.1 Effect of precorrosion

a) 6013-T6

Precorrosion has a strong initial effect since initiation lives are reduced by a factor of 2 as seen in table 13. Table 14 displays the reductions in total fatigue lives. Extending the precorrosion time does not strongly affect the initiation and propagation lives in the limits of accuracy.

Stress range	As received/ in air	6/G69 in air	12/G69 in air	24/G69 in air	As received in G69
100 MPa	100%	49.1%	41.7%	46.0%	21.1%
120 MPa	100%	60.1%	42.5%	41.2%	25.1%
140 MPa	100%	48.2%	40.1%	48.6%	28.5%

Table 13: 6013-T6 alclad TL: Initiation life after precorrosion
Chamfer hole, RT, f=10 Hz, R=0.05

57

Stress range	As received/ in air	6/G69 in air	12/G69 in air	24/G69 in air	As received in G69
100 MPa	100%	61.2%	52.1%	58.3%	29.8%
120 MPa	100%	61.6%	60.8%	52.5%	31.6%
140 MPa	100%	55.9%	46.6%	56.9%	31.7%

Table 14: 6013-T6 alclad TL: Fatigue life after precorrosion
Chamfer hole, RT, f=10 Hz, R=0.05

Propagation lives are slightly affected by precorrosion. This explains the decrease in the ratio of initiation life to total life with precorrosion as seen in table 15.

Stress range	ratio	As received in air	6/G69 in air	12/G69 in air	24/G69 in air	As received in G69
100 MPa	initiation/total	65.89%	52.88%	52.82%	52%	46.59%
120 MPa	initiation/total	66%	64.85%	46.41%	52%	52.92%
140 MPa	initiation/total	72%	62.57%	62.30%	62%	65.20%

Table 15 : 6013-T6 alclad TL: Ratio of initiation life to total life.
Chamfer hole, RT, f=10 Hz, R=0.05

S-N curves are presented in figures 5.3-5.4. They confirm the data given by tables 13-15 and show that 6013-T6 alclad is inferior to 2024-T3 alclad when tested in air. A summary of the precorrosion and stress effects on 6013-T6 fatigue behavior is displayed in Fig.5.5-5.6 . Propagation lives are unchanged whereas initiation lives are decreased by precorrosion. An increase in stress level lowers both initiation and propagation lives.

b) 2024-T3 alclad versus 6013-T6 alclad

S-N curves for 2024-T3 alclad are shown in Fig.5.7-5.8. Tables 16-17 display the initiation and fatigue lives of 2024-T3 alclad after precorrosion.

Stress range	As received/ in air	6/G69in air	12/G69 in air
120 MPa	100%	100%	47.0%
140 MPa	100%	54.7%	37.8%
170 MPa	100%	60.2%	79.2%

Table 16: 2024-T3 alclad TL: Initiation life after precorrosion
Processed from D.Steul MIT Thesis [45]

Stress range	As received/ in air	6/G69in air	12/G69 in air
120 MPa	100%	89.0%	51.7%
140 MPa	100%	74.3%	70.3%
170 MPa	100%	86%	100%

Table 17: 2024-T3 alclad TL: Fatigue life after precorrosion
Processed from D.Steul MIT Thesis [45]

Total lives are slightly decreased while initiation lives are reduced by almost a factor of 2. In any case, the effect of precorrosion is less than for 6013-T6 alclad.

IV.1.2 6013-T6 alclad: effect of rivet hole geometry

As seen in Fig.5.9, the rivet hole geometry has little effect on the fatigue lives of the precorroded and as received specimens tested in air.

IV.1.3 6013-T6 alclad: Tests run in ASTM G69

Before fatigue crack initiation starts, an intense hydrogen evolution around the hole is observed. The bubbles are confined to a zone having the a shape similar to the plastic zone. Chamfer hole specimens exhibit a lower fatigue resistance than straight hole specimens as seen in Fig.5.10.

IV.1.4 Cladding effect

The detrimental effect of the cladding is shown in Fig.5.11. The stress concentration factor k_t for a straight open hole was evaluated from [37] as 2.8. The bare material data is taken from Alcoa. The cladding clearly has a detrimental effect on the total life of the notched component.

59

IV.1.5 Fractography

a) 6013-T6 alclad

Fracture surfaces are examined under the SEM. Numerous pits are found on the fracture surface of precorroded specimens (Fig.5.13-5.14). Evidence of intergranular corrosion is also found occasionnaly (Fig.5.13). However, crack initiation is always transgranular, despite the presence of some crystallographic facets which are expected during stage I growth.Microcracks linking pits together are observed below the fracture surface (Fig.5.15). Microcracks initiating from the cladding and/or at the cladding/core metal interface are also seen, in both straight hole and chamfer hole specimens (Fig.5.16-5.17). The fracture surface of specimens tested in solution do not exhibit pits.

b) 2024-T3 alclad

Corrosion damage on the countersink where no cladding protects the base metal is found but is not serious [45]. This confirms the observation that few pits are found on cross-sections.
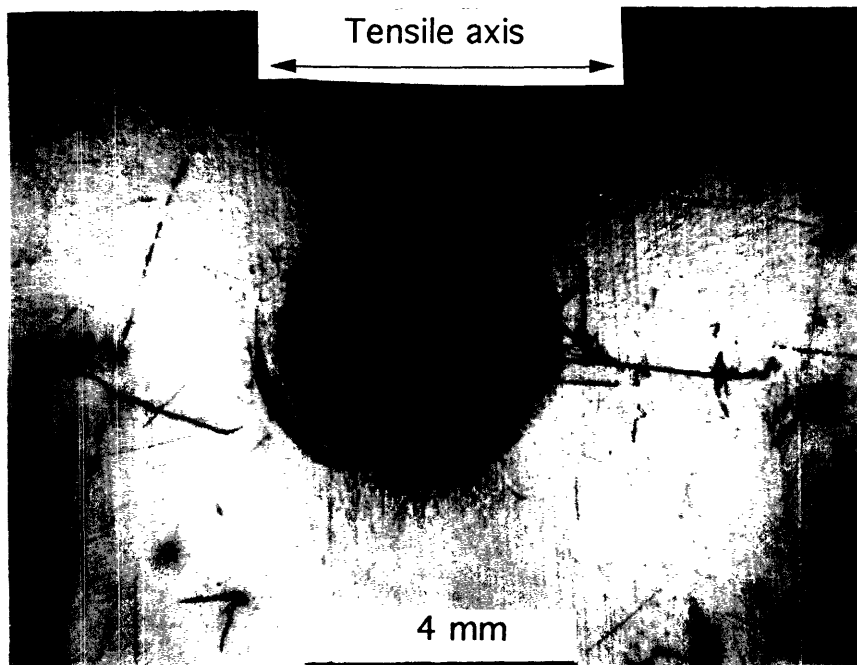
Fig.5.1: 6013-T6 alclad: Optical micrograph of the chamfer edge. Microcracks perpendicular to the tensile axis can be seen on both sides of the hole. As received specimen. $\Delta\sigma$=100MPa, 70,000 cycles, 10 Hz, RT, R=0.05, tested in air (x8.75)
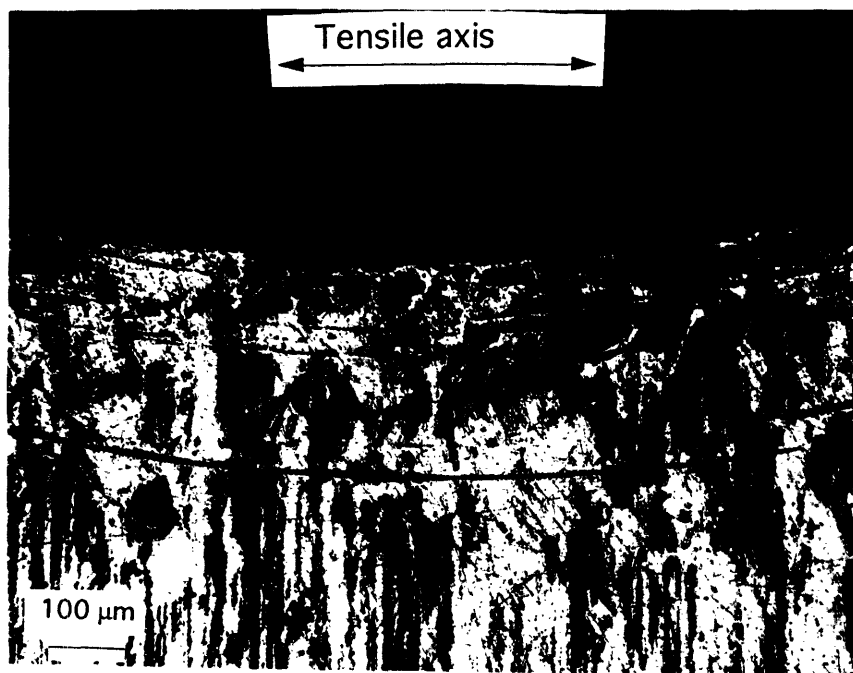
Fig.5.2: 6013-T6 alclad: Optical micrograph of the chamfer edge. Enlarged view of the previous micrograph. Large deformation bands (perpendicular to the tensile axis) and slip bands (45° from the tensile axis) are visible . Circles are machining marks (x100)

N_i(Number of cycles to a crack length of 0.4 mm)
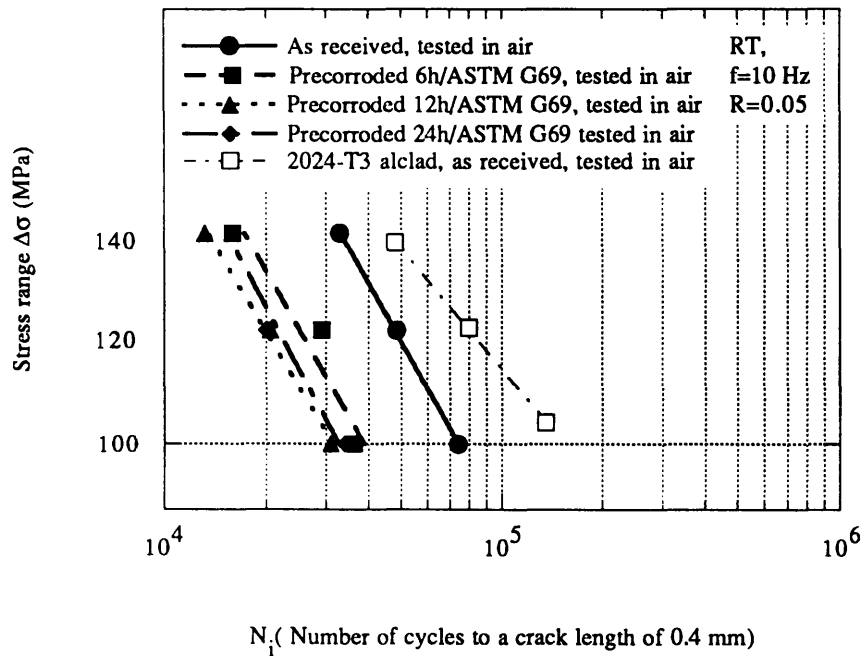
Fig.5.3: Effect of precorrosion on fatigue crack initiation life of 6013-T6 aluminum alloy, Chamfer hole

N_f (Number of cycles to failure)
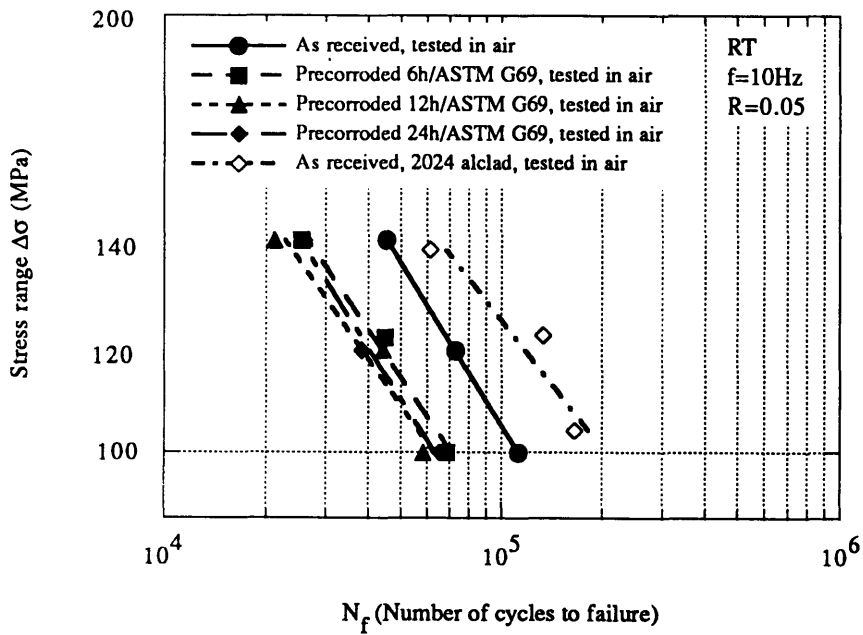
Fig.5.4: Effect of precorrosion on fatigue life of 6013-T6 aluminum alloy Chamfer hole

Effect of precorrosion on initiation and propagation lives
for 6013-T6 Alclad aluminum alloy.
Δσ=100 MPa, Chamfer hole.
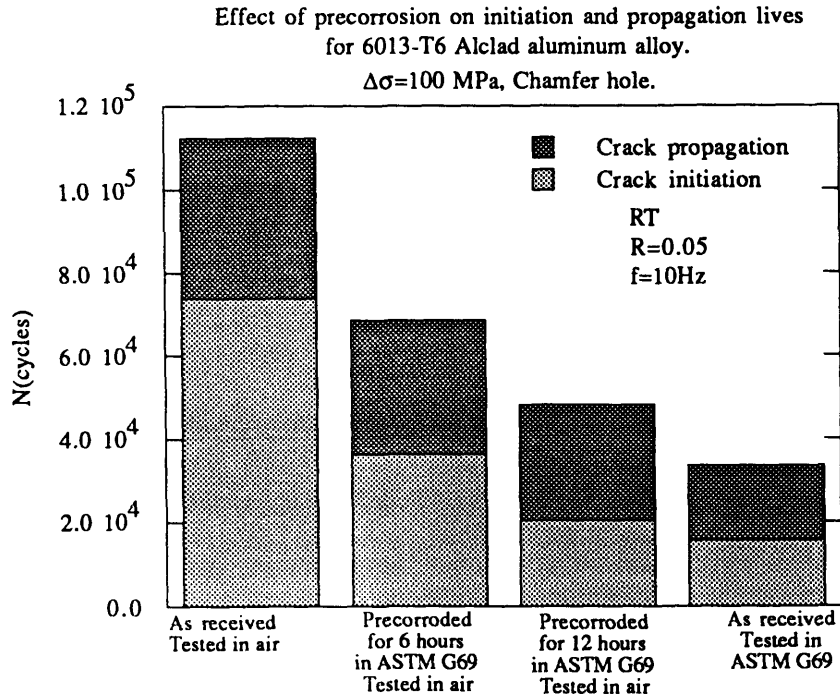
Fig.5.5: Effect of experimental conditions on initiation and propagation lives
of 6013-T6 alclad aluminum alloy, chamfer hole, Δσ=100MPa
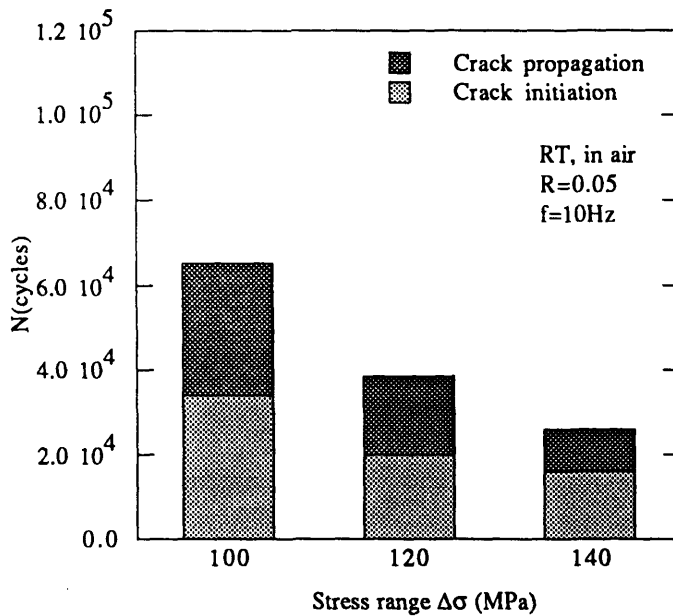
Fig.5.6: Effect of stress on initiation and propagation lives of 6013-T6 alclad
aluminum alloy, chamfer hole, precorroded for 24 hours in ASTM G69

63
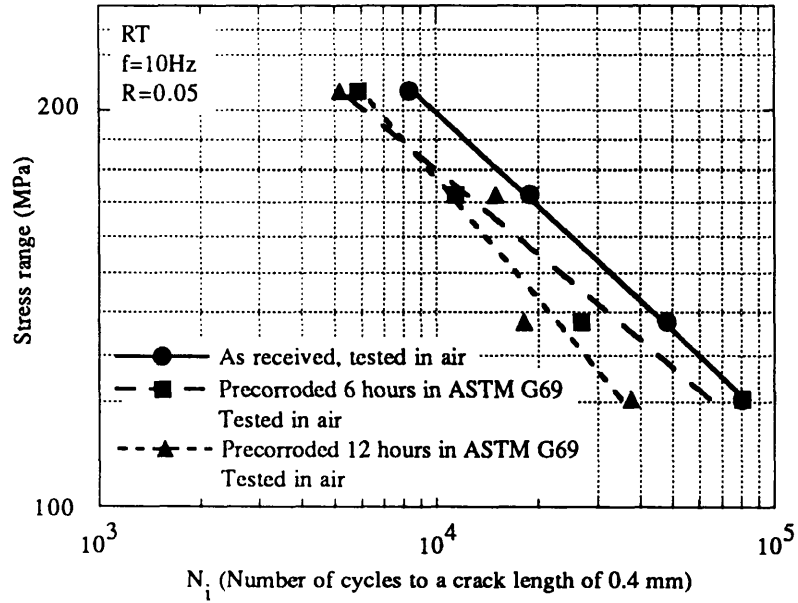
Fig.5.7: Effect of precorrosion on initiation life of 2024-T3 alclad aluminum alloy
Chamfer hole
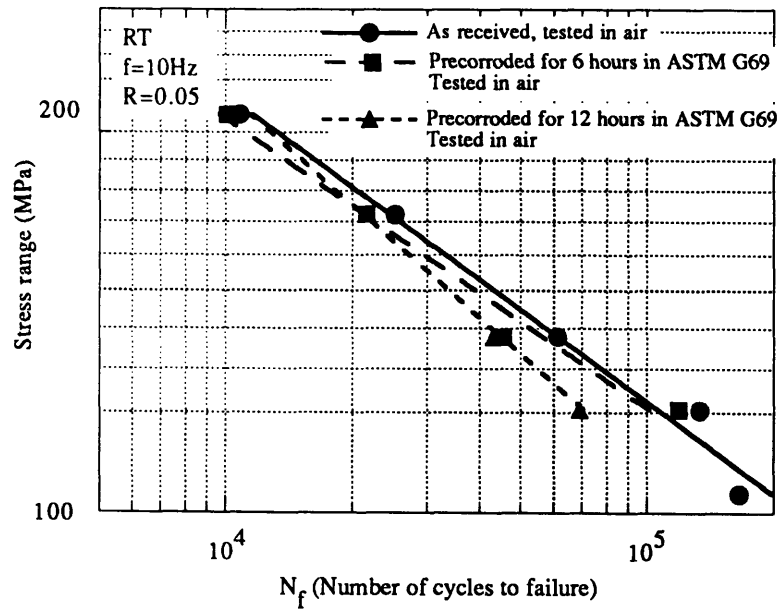
Fig.5.8: Effect of precorrosion on fatigue lives of 2024-T3 alclad aluminum alloy
Chamfer hole
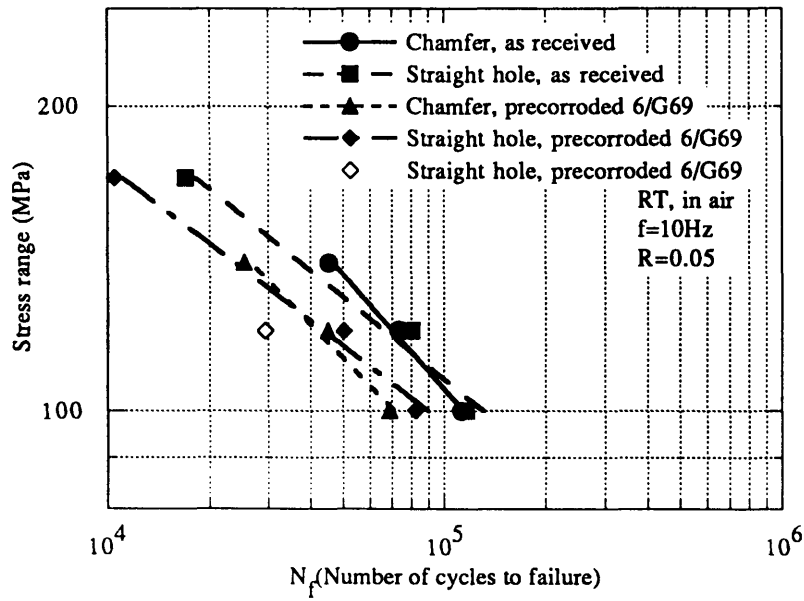
Fig.5.9: 6013-T6: S-N curves
Straight hole versus chamfer hole
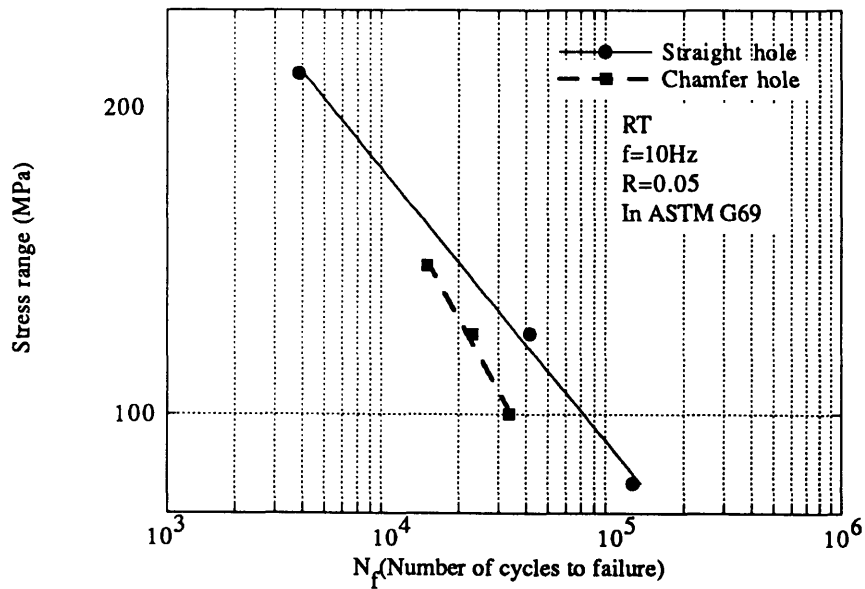
Fig.5.10: 6013-T6: S-N curves
Straight hole versus chamfer hole

65
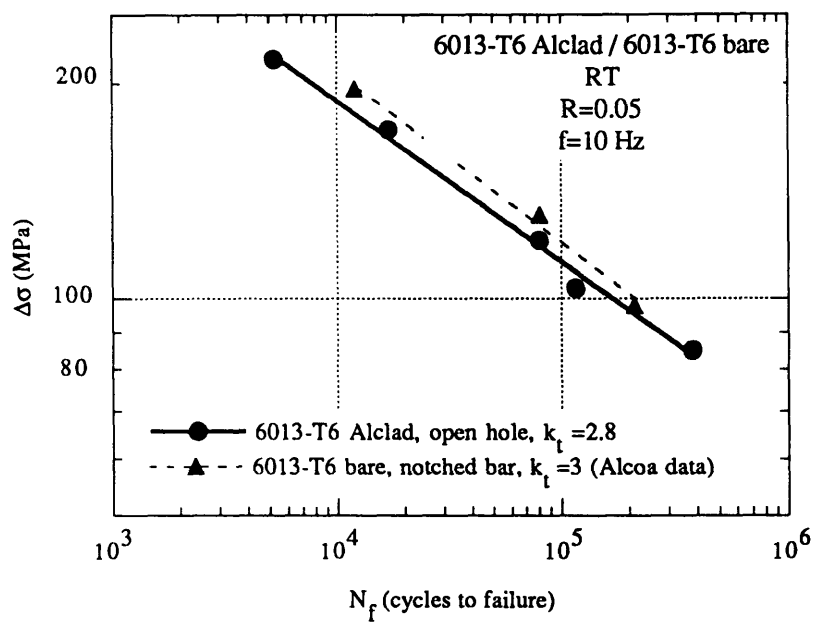
Fig.5.11: S-N curve: 6013-T6 bare versus alclad.
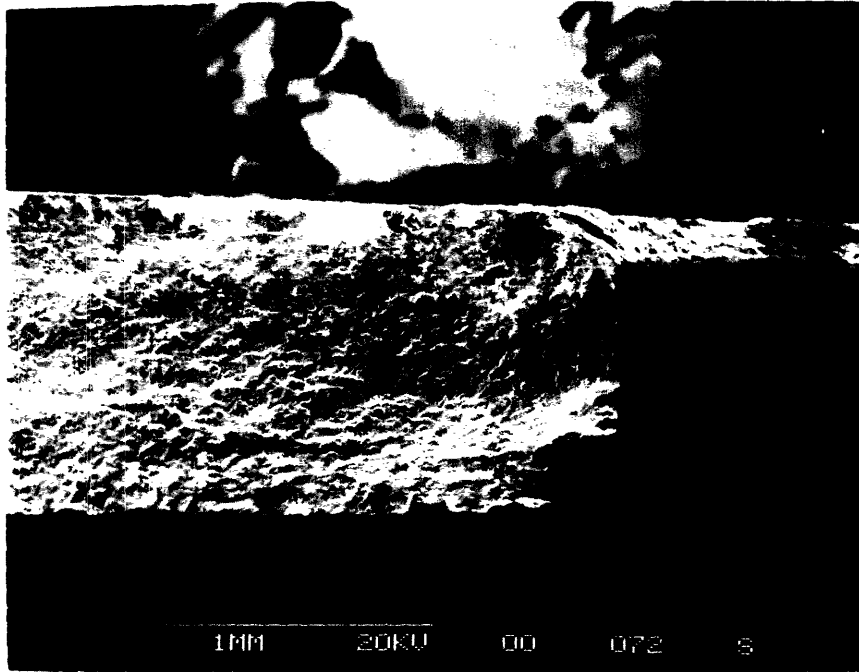
Fig.5.12: SEM micrograph of 6013-T6 alclad. Straight hole. Precorroded for 6 hours in ASTM G69. Fatigue tested in air. $\Delta\sigma$=120MPa. (x36)

Zone of
crack initiation

Intergranular
Corrosion
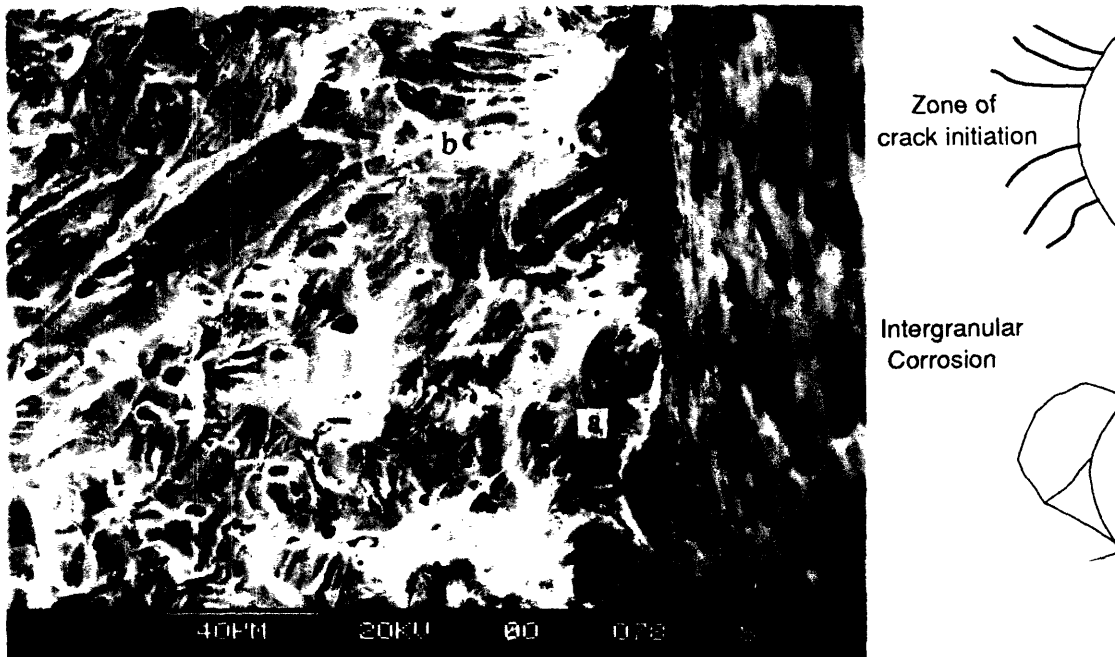
Fig.5.13: SEM micrograph of 6013-T6 alclad. Precorroded for 6 hours in ASTM G69. Fatigue tested in air. $\Delta\sigma$ =120 MPa. Straight hole. Some intergranular corrosion can be seen in area (a). A crack initiate from area (b). (x490)

67
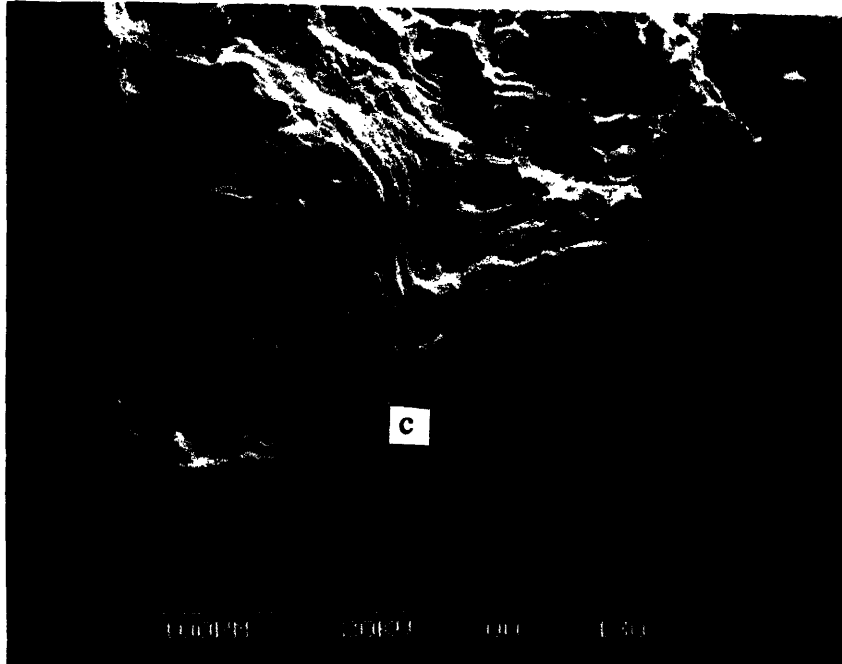
Fig.5.14: SEM micrograph of 6013-T6 alclad. Numerous pits can be seen on the fracture surface. A crack initiated from area (c). Precorroded 6 hours in ASTM G69. Fatigue tested in air. $\Delta\sigma$=120 MPa(x360)
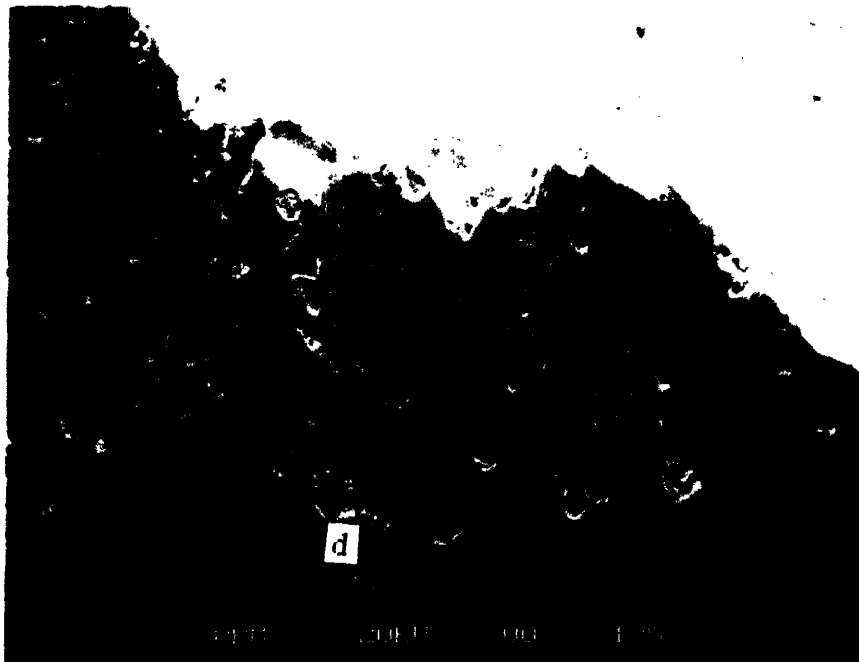
Fig.5.15: SEM micrograph of 6013-T6 alclad. A microcrack links two pits in area (d) Precorroded 6 hours in ASTM G69. Fatigue tested in air. $\Delta\sigma$ =120MPa (x360)
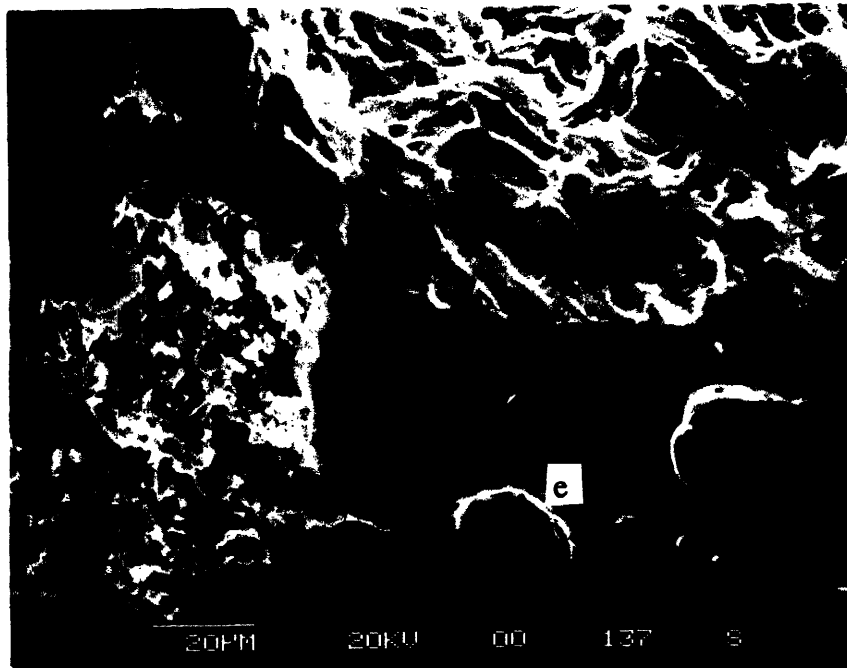
Fig.5.16: SEM micrograph of 6013-T6 alclad. Straight hole. Precorroded for 6 hours in ASTM G69. Fatigue tested in air. Δσ=120 MPa. A crack initiates from the pitted cladding and goes through a pit in area (e) (x700)

Fig.5.17: SEM micrograph of 6013-T6 alclad. Chamfer hole. Precorroded for 6 hours in ASTM G69. Fatigue tested in air. Δσ=120MPa. Microcracks can be seen in area (f) at the cladding/base metal interface. (x700)

V.2 Crack propagation

Fatigue crack growth data are recorded as 2a (crack length) versus N (number of cycles) and are processed according to the seven point polynomial approximation [46] which gives da/dN as a function of ΔK, the stress intensity factor which is given as follows :

$$\Delta K = \Delta\sigma \sqrt{\sec(\tfrac{\pi a}{w})} \ \sqrt{\pi a}$$

where Δσ the stress range and w the sample width.

Fig.5.18 shows a graph of 2a versus N for an as received specimen tested in air.

V.2.1 Effect of load ratio

The R-ratio effect is seen in Fig.5.19. The effect is stronger for 6013-T6 than for 2024-T3, in all experimental conditions. 2024-T3 alclad is slightly better than 6013-T6 alclad. Since it is reported that 6013-T6 bare is slightly better than 2024-T3 at high ΔK [8], then it seems that the cladding has a detrimental behavior on crack propagation.

V.2.2 Precorrosion

Even though the cladding exhibits an abnormal pitting behavior, the results are relevant since in real service life conditions, corrosion takes place on one side, namely along the adhesive bond. As seen in Fig.5.20, precorrosion caused no detrimental effect for times less than 24 hours in the limit of test accuracy, and might be beneficial. This behavior is due to the aluminum cladding which does not bear the load. Because of its softness, it has a detrimental effect on fatigue cracking. Pitting destroys the cladding and can reduce the available crack length in the cladding which impedes crack propagation to the base metal. In this case, the pitted band must be contained in the plane of the crack. However, for long precorrosion time, crack growth is slightly increased when
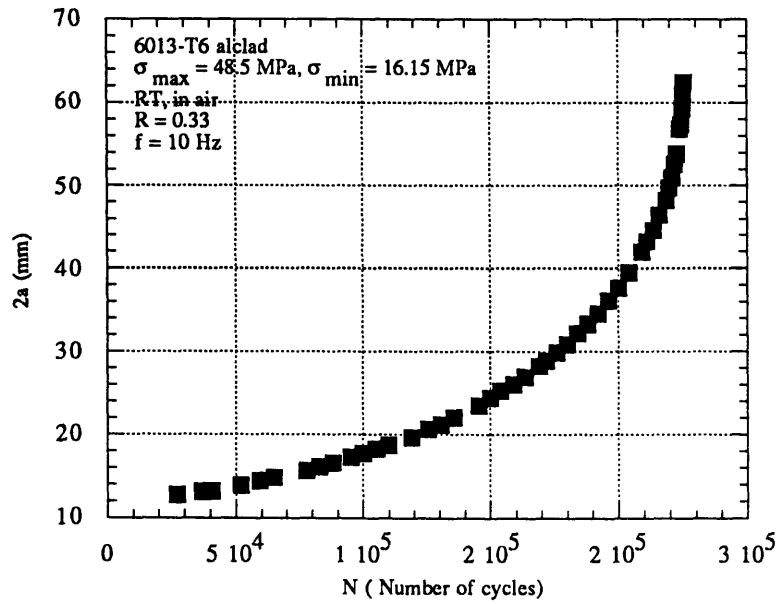
Fig.5.18 : 6013-T6 alclad: crack length versus number of cycle
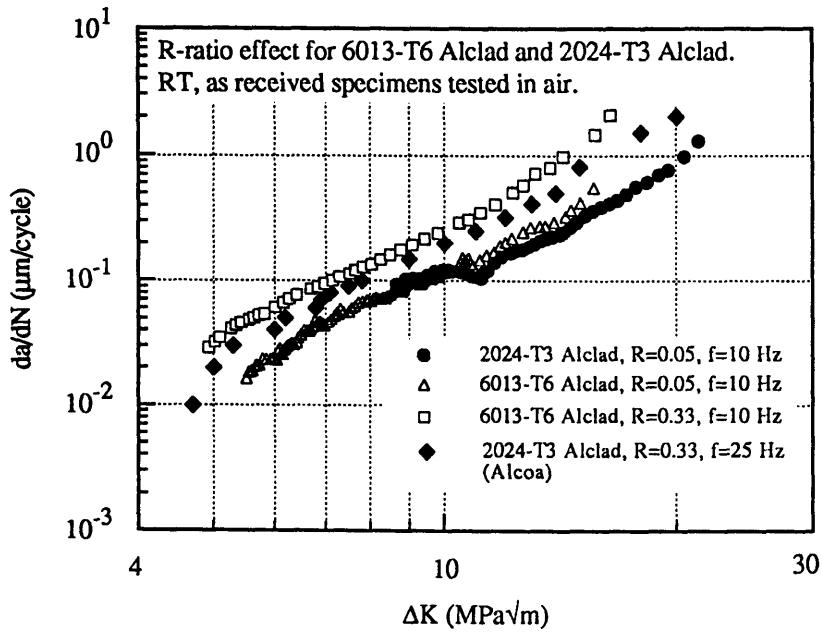
Fig.5.19: R-ratio effect on 2024-T3 alclad and 6013-T6 alclad

71
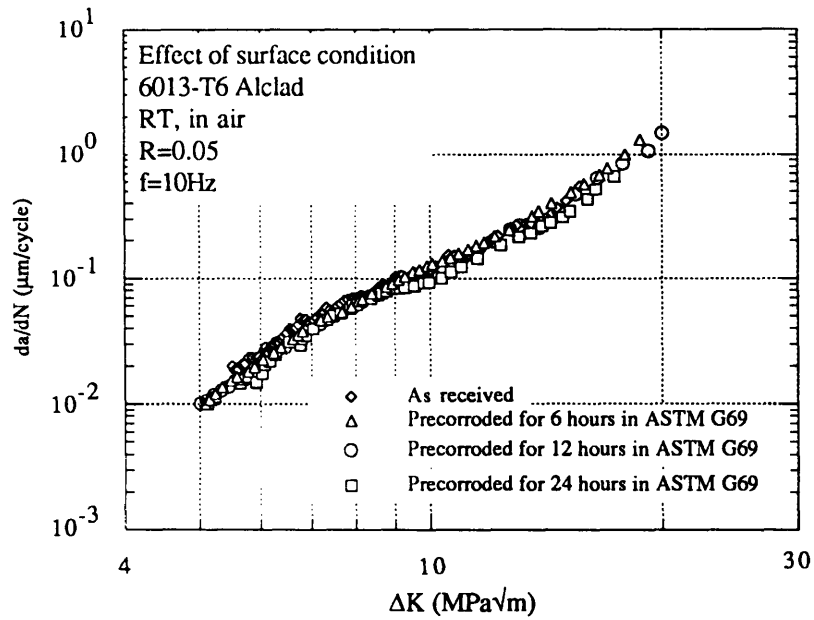
Fig.5.20: Effect of precorrosion on the crack growth rates of 6013-T6 alclad
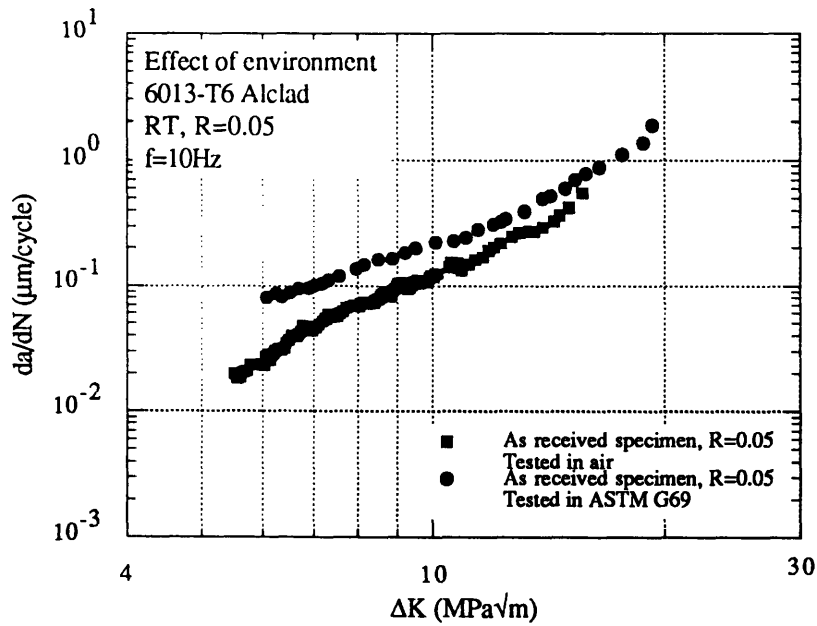
Fig.5.21: Effect of the environment on crack growth rates of 6013-T6 alclad

compared to as received specimens. A metallographic examination of the cross-section shows that the cladding has been totally removed at some locations, but no evidence of corrosion damage is seen on the core metal.

V.2.3 ASTM G69

Tests run in ASTM G69 show a sharp increase in crack growth rates at low ΔK. A factor of 1.7 is evaluated at $\Delta K = 6$ MPa$\sqrt{m}$ in Fig.5.21. At high ΔK, the curves for tests run in air and in solution are roughly the same. This is observed for both R-ratios. The increase at low crack growth rates is explained by the synergistic effect of corrosion and fatigue. At high crack growth rates, the environment does not have time to interact. This increase in crack growth rates shows that the cladding cannot fully protect the base metal, as seen before in the pitting studies.

V.2.4 Frequency effects

To evaluate the effect of frequency on tests run in solution, the frequency is reduced to 0.1Hz. An increase of crack growth rates is expected at low ΔK. On the contrary, a decrease is recorded. This is probably due to crack blunting and crack branching as mentioned by D.Steul [45].

III. Fractography

Fracture surface are examined with an SEM. In Fig.5.22, crystallographic facets characterizing stage I growth can be observed on specimens tested in air. However, crack propagation is fully transgranular at higher ΔK. Beach marks are clearly visible. A constituent particle can be seen at the bottom of a dimple, exhibiting brittle behavior (Fig.5.23).

Examination of the fracture surfaces of specimens tested in solution is hindered by corrosion products. In addition, active dissolution has removed the beach marks at low

ΔK. Particles are still visible at the bottom of the pits that have been created by ASTM

G69 solution during crack propagation (Fig.5.24). At high ΔK, beach marks still appear

on the fracture surface because the environment does not have time to alter the surface.

Mudlike patterns are clearly visible and secondary cracking can be observed (Fig.5.25)
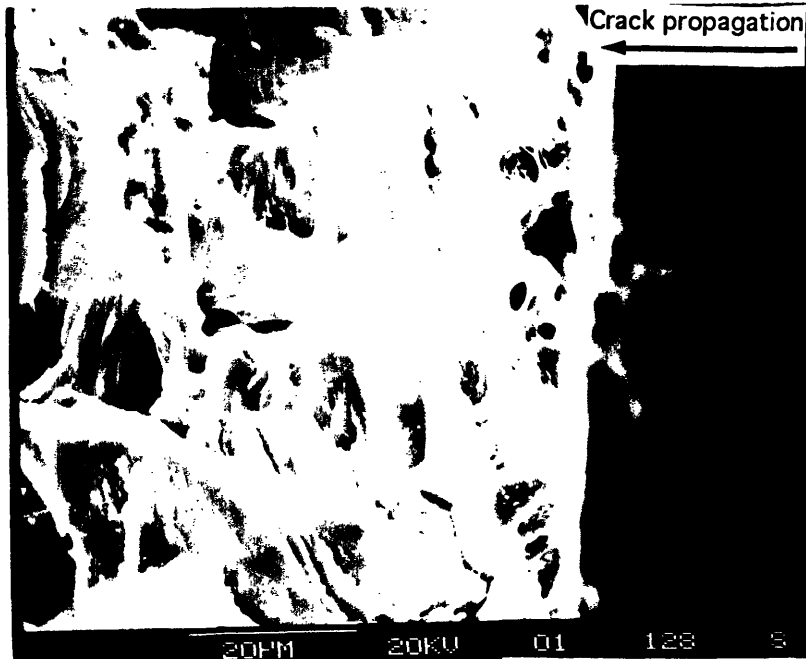
Fig.5.22: SEM micrograph of 6013-T6 alclad. Stage I crack growth. Crack path is rough and characterized by some crystallographic facets. CCT specimen precorroded for 12 hours in ASTM G69, R=0.33, low DK. $\Delta\sigma$=32.4 MPa (x1100)
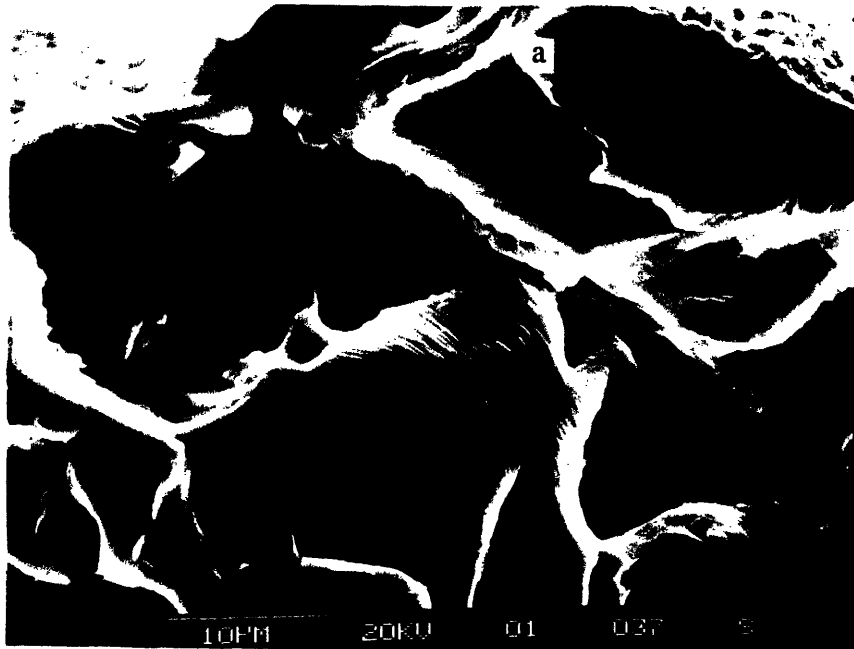
Fig.5.23: SEM micrograph of 6013-T6 alclad. Stage II crack growth. Crack propagation is transgranular. In area (a), a particle can be detected at the bottom of a dimple. CCT specimen precorroded for 24 hours in ASTM G69, R=0.33, low ΔK, $\Delta\sigma$= 32.4 MPa (x2100)
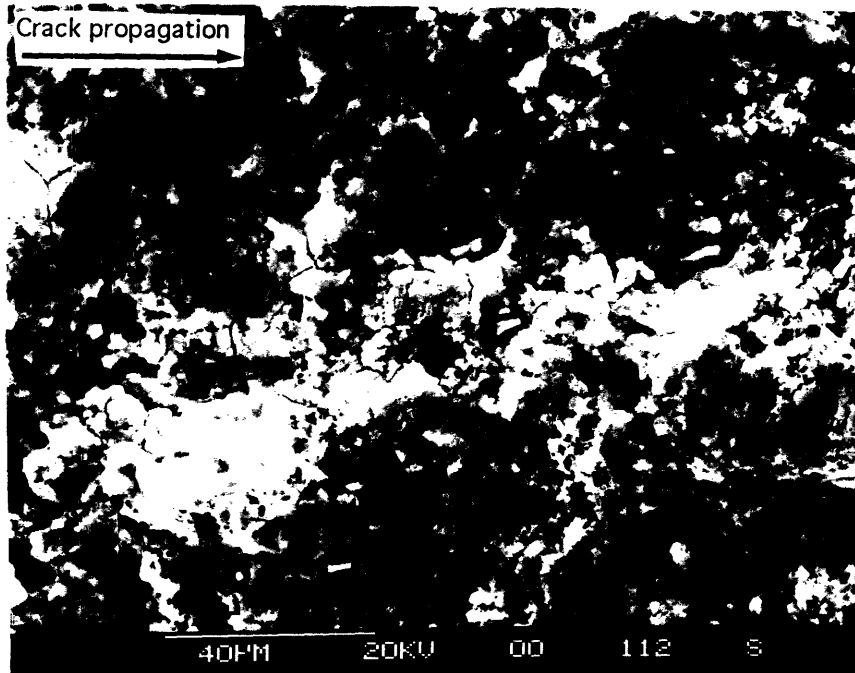
Fig.5.24: SEM micrograph of 6013-T6 alclad. As received specimen tested in ASTM G69.R=0.05. Δσ=104 MPa. Low ΔK. Fatigue striations are dissolved or covered by corrosion products. Many particles can be seen at the bottom of the pits (x675)
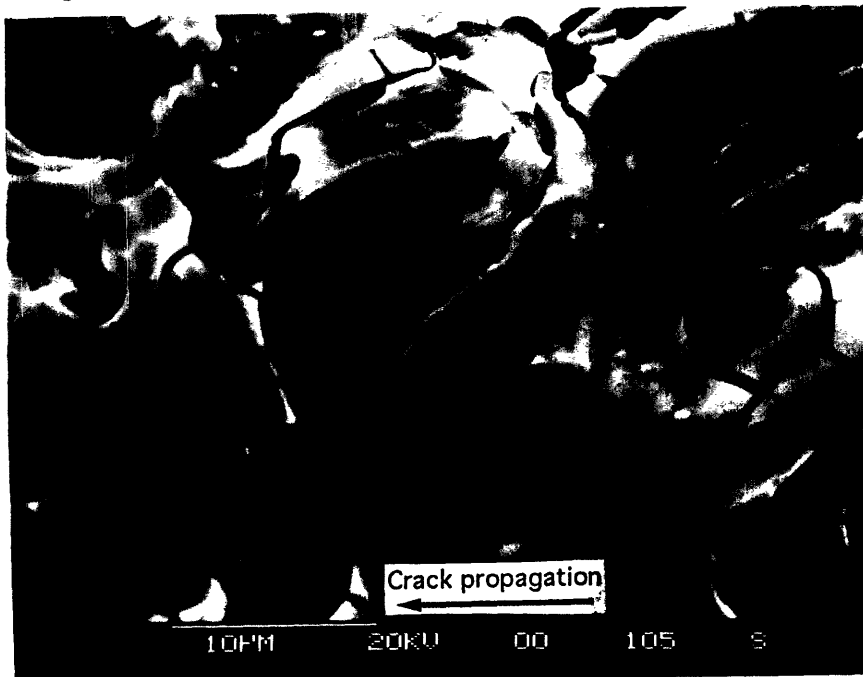
Fig.5.25: SEM micrograph of 6013-T6 alclad. As-received specimen tested in ASTM G69. R=0.05, Δσ=104 MPa. High ΔK. Corrosion products form mudlike patterns. Crack propagation is still transgranular. (x2700)

VI. Discussion

1) Fatigue performance in air

6013-T6 alclad is inferior to 2024-T3 alclad both in the as-received and precorroded condition in terms of fatigue performance. One cannot directly compare fatigue crack propagation lives for the two alloys since some uncertainties remain. By assuming that crack growth rates are equal, which is not a bad approximation, it can be deduced that the inferiority of 6013-T6 alclad fatigue performance lies in the crack initiation lives. Grain shape and size may play a role in fatigue crack initiation. Slip bands are probably more constrained by flattened grain boundaries (2024-T3) than in almost equiaxed grains (6013-T6). In addition, cladding thickness can also play a role in fatigue crack initiation. In 6013-T6 alclad, the cladding is 10% of the total thickness whereas the specifications for 2024-T3 alclad require 5% [47]. Moreover, tensile strength of 2024-T3 is 13% higher than 6013-T6.

2) Pitting behavior and its effects on corrosion fatigue crack initiation lives

In 6013-T6 alclad, crystallographic pits in the cladding do not extend over a distance larger than 50 µm in the T-direction. Cross-sections of 6013-T6 alclad sheet show that the base metal is cathodically protected when the cladding is removed over such a length. However, the cladding is not efficient enough to completely protect the base metal which is exposed to ASTM G69 by the rivet hole. This is illustrated by pits which initiate around second phase particles. The corrosion is less dramatic in 6013-T6 alclad than in 6013-T6 unclad since severe intergranular corrosion, along with pitting, is observed when 6013-T6 unclad is exposed to salt water solutions [7]. This is also observed in 2024-T3 where the cladding sharply reduces the extent of pitting corrosion both in terms of pit depth and pit density, even if pits in 2024-T3 alclad are still deeper

than in 6013-T6 alclad. In addition, pit density is extremely low in 2024-T3 alclad while it is quite high in 6013-T6 alclad. It is also observed that 2024-T3 cladding dissolves readily in a corrosive environment whereas 6013-T6 cladding corrodes by pitting. This demonstrates a difference in the effectiveness of cathodic protection in the two alloys.

Fractographic analysis of 6013-T6 alclad shows numerous pits on the fracture surface. Below the fracture surface, one may observe microcracks which link pits together. Microcracks at the cladding/core metal interface and cracks initiating from the cladding can be seen. Fatigue cracking of precorroded specimens is due to both the detrimental effect of the cladding and pitting. However, since the cladding is not severely damaged and a sharp reduction in fatigue life is recorded, the effect of pitting on fatigue crack initiation of 6013-T6 alclad is predominant.

Cross-sections of 2024-T3 alclad exhibit only very few pits, a maximum of two over a thickness of 1 mm. Fatigue cracking always initiates at the countersink. If pitting plays a role in 2024-T3 alclad fatigue cracking, the fatigue resistance depends on the location of the critical pit which will induce cracking. The probability of finding a pit at a critical location is less in 2024-T3 alclad than in 6013-T6 alclad. Thus, 2024-T3 alclad fatigue crack initiation is more resistant to corrosion than 6013-T6 alclad initiation life.

3) Dependence of fatigue lives on precorrosion times

Fig.6.1-6.2 show the dependence of initiation and fatigue lives with the maximum pit depth, as determined from Chapter 3. Very little variation is recorded between 6, 12 and 24 hours exposure time.

Modeling a pit as a semi-elliptical crack on the edge of a rivet hole [36], the stress intensity factor is given by:

$$\Delta K = 1.12 \, \Delta\sigma \sqrt{\frac{\pi c \, \alpha}{Q}}$$

where c is the pit radius, a the pit depth and α is the aspect ratio equal to a/c. The shape factor, Q is equal to $1+ 1.464 \alpha^{1.65}$.

With respect to pitting kinetics, two limiting cases can be investigated. The first deals with pit coalescence; pits grow in area but not in depth. The second case is characterized by pit growth in depth but not in area.

a) Pit growth in area

Pits coalesce to form larger pits with a lower aspect ratio (depth/radius). In this case, the stress intensity factor increases as seen in Fig.6.3. A zero aspect ratio corresponds to a through crack on the edge of a rivet hole.

b) Pit growth in depth

When the pit depth increases faster than pit radius, the aspect ratio increases. The stress intensity factor goes through a maximum at constant diameter and then falls slowly. This is shown in Fig.6.4. There is also a sharp increase in the stress intensity at a low aspect ratio. In this case, if a defect covers a large area, e.g a particle, the stress intensity factor grows sharply in the early stages of dissolution. Assuming a critical ΔK for fatigue crack initiation from a pit, the initiation life is reduced strongly within the first microns of pitting depth.

In 6013-T6 alclad, the stress intensity factor at the tip of the pits is described by the second mechanism. In fact, pit diameters vary very little with precorrosion time (Fig.3.3-3.4) and pit depth follows a power law dependence on precorrosion times. Thus, the stress intensity factor at the tip of the pits should not change too much. This is confirmed by the results which show that extending the precorrosion time does not decrease the fatigue life at the same rate.

It is reported by N.L.Person [42] that the first 3 mils (0.08mm) of pitting are very detrimental to the fatigue strength of 2014, 5083 and 7075 aluminum alloy. Enhancing

pitting only slightly decreases the fatigue properties. In addition, at long corrosion times, pits cannot be considered isolated. since pit density increases sharply. (Fig.3.7). Howevre, it is unknown how the individual stress concentrations affect each other.

4) Propagation lives and initiation lives of precorroded specimens

Fatigue cracks initiate at the bottom of pits located on the chamfer hole of precorroded specimens. Fatigue crack propagation lives are calculated by integrating da/dN curve from the initial crack length to the final crack length. The initial crack length is taken as the maximum pit depth given by the precorrosion. The final crack length is a_c, which delimits the fatigue crack propagation phase from the unstable fracture phase. a_c is load dependent. From the results of the previous chapter, da/dN curve for 6013-T6 alclad at an R-ratio of 0.05 can be approximated by: $da/dN=1.326 \times 10^{-7} (\Delta K)^{2.97}$ mm/cycle, where ΔK is in MPa$\sqrt{m}$.

Fatigue crack propagation is divided into three phases. The first accounts for the notch effect of the hole. The corresponding short crack stress intensity factor is determined by:

$$\Delta K = 1.12 \, \Delta\sigma \, k_t \sqrt{\pi l}$$

k_t is the stress concentration factor due to the hole and is estimated at 2.8 for a straight hole. l is defined in Fig.6.5. D, the hole diameter is 4 mm. There is no short crack growth problem other than the one induced by the notch since pit depth is larger than grain length. The second and third phases are governed by a long crack stress intensity factor:

$$\Delta K = \Delta\sigma \frac{\sqrt{\pi a}}{\sqrt{\cos\left(\frac{\pi a}{w}\right)}}$$

$\Delta\sigma$ is the applied stress range and a is defined in Fig.6.6. Transition from phase I to phase II defines a critical length which is calculated by equating ΔK_{long} to ΔK_{short}. One finds a critical length of 0.23 mm. Phase II and III represent a single fatigue crack propagation phase. Phase III is introduced to compare calculated propagation lives with experimental crack propagation lives as determined by defining fatigue crack initiation

80

as a crack length of 0.4 mm. Table 18 summarizes the different fatigue crack propagation regimes:

	Phase	Start	Finish	ΔK (MPa$\sqrt{m}$)
Short crack (notch)	I	pit depth	0.23 mm	$\Delta K=1.12\Delta\sigma K_t\sqrt{\pi l}$
Long crack	II	2.23 mm	2.4 mm	$\Delta K=\Delta\sigma\dfrac{\sqrt{\pi a}}{\sqrt{\cos\left(\frac{\pi a}{w}\right)}}$
Experimental/calculated	III	2.4 mm	a_c	$\Delta K=\Delta\sigma\dfrac{\sqrt{\pi a}}{\sqrt{\cos\left(\frac{\pi a}{w}\right)}}$

Table 18: Limits of the three stages of crack propagation

Results are displayed in Table 19 for 6 hour precorrosion. Pit depth is taken as the maximum pit depth determined in Chapter II. Phase III shows a good correlation with the experimental values(Fig.6.7). Experimental values are calculated by averaging the propagation lives of specimens with different precorrosion time but tested under the same stress range.

$\Delta\sigma$	Phase I	Phase II	Phase III	Experimental III	Total
100 MPa	15102	2174	36317 (a_c=14 mm)	32413 cycles	47250
120 MPa	8787	1265	19827 (a_c=13mm)	20624 cycles	27041
140 MPa	5559	800	12353 (a_c=12mm)	9961 cycles	16736

Table 19: 6013-T6 alclad: Calculated propagation lives (chamfer hole)

From the total propagation lives, initiation lives are deduced by subtracting propagation lives from experimental total lives. Table 20 presents the results for 6, 12 and 24 hour precorrosion in ASTM G69. Pit depth is the initial crack length.

	$\Delta\sigma$	Initiation life	Propagation life	Total life
6/G69	100 MPa	16416	52303	68719
Pit depth	120 MPa	15145	29879	45024
19 µm	140 MPa	6696	18712	25408
12/G69	100 MPa	8793	49684	58477
Pit depth	120 MPa	16082	28355	44437
25 µm	140 MPa	3438	17748	21186
24/G69	100 MPa	18019	47383	65402
Pit depth	120 MPa	11334	27017	38351
32 µm	140 MPa	8950	16901	25851

Table 20: 6013-T6 alclad: Calculated fatigue crack initiation and propagation lives in number of cycles. R=0.05, precorroded in ASTM G69, f=10Hz, R=0.05, tested in air, chamfer hole.

81

Total lives cannot be estimated by only assuming that pitting damage act as an initial through crack since the estimation is too conservative. One notices an important scatter in fatigue initiation lives because this model transfers the scatter of total lives to initiation lives without accounting for any scatter due to the propagation lives. In addition, as defined propagation lives are no longer independent from the precorrosion times since a different initial crack length is assumed for each precorrosion time.

5) Tests in ASTM G69

No pitting is distinct. The longest time spent in ASTM G69 solution before crack initiation is 15606 cycles, that is 1560 seconds or 0.43 hours. This corresponds to a theoretical maximum pit depth, in free corrosion, of 6.76 µm. This is a shallow pit as confirmed in Fig.3.3. Stress concentration at the tip of the pit cannot alone account for the sharp decrease in fatigue and initiation lives. Another mechanism of corrosion fatigue must occur. The intense hydrogen evolution seen around the hole on the cladding may be the sign of the phenomenon of localized plasticity and anodic dissolution [38]. In this case, fatigue initiation cannot be predicted on the basis of a critical pit depth.
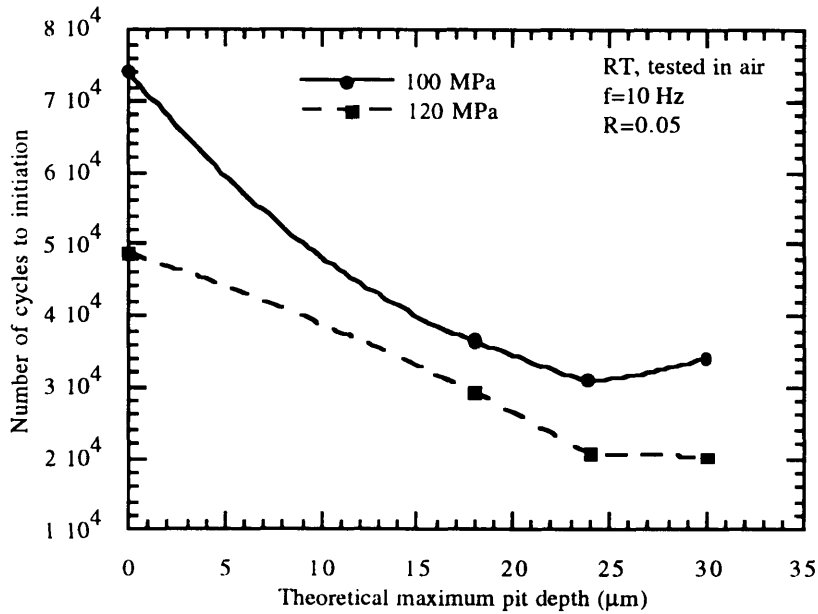
Crack initiation is defined as the number of cycles necessary to grow a crack of length 0.4 mm

Fig.6.1: 6013-T6 alclad: Number of cycle to initiation as a function of the maximum pit depth.
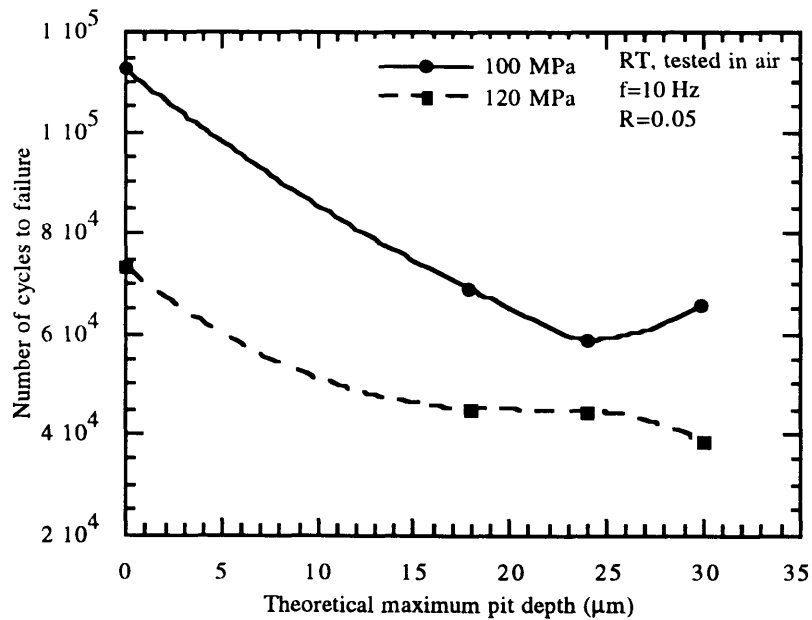
Fig.6.2: 6013-T6 alclad: Number of cycles to failure as a function of the maximum pit depth.
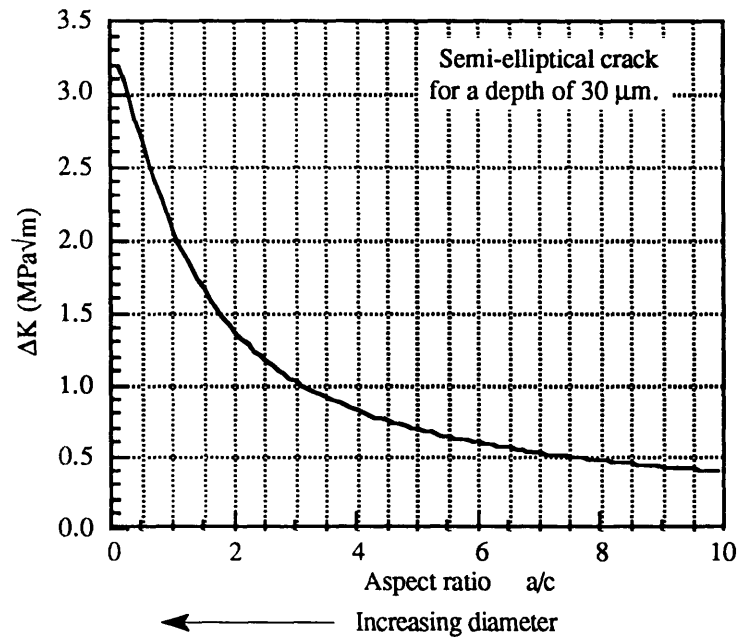
Fig.6.3: Semi-elliptical crack at the edge of a rivet hole: Stress intensity factor as a function of the aspect ratio. Depth: 30 μm. Δσ=100 MPa. k_t=3.
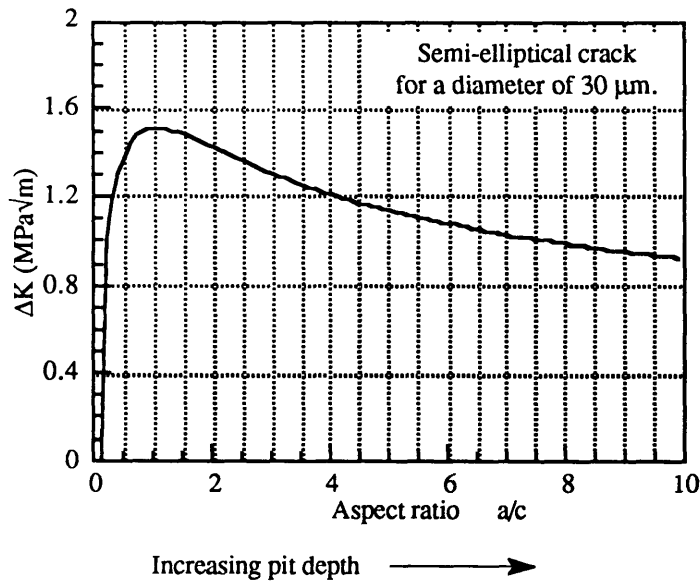
Fig.6.4: Semi-elliptical crack at the edge of a rivet hole: Stress intensity factor as a function of the aspect ratio. Diameter: 30 μm. Δσ=100MPa. k_t=3.
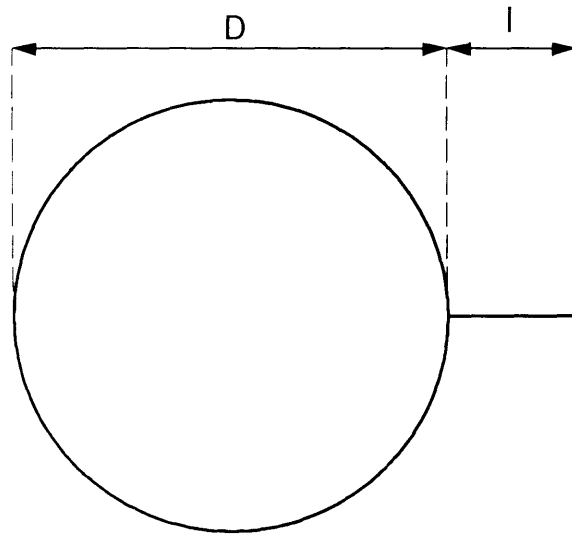
Fig.6.5: Short crack configuration

2a
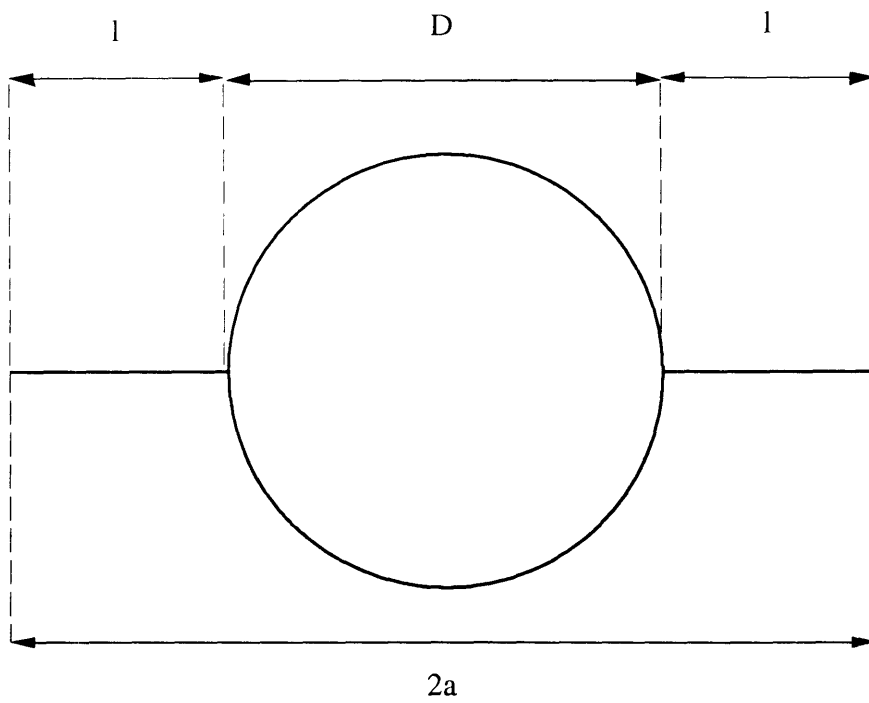
Fig.6.6: Long crack configuration
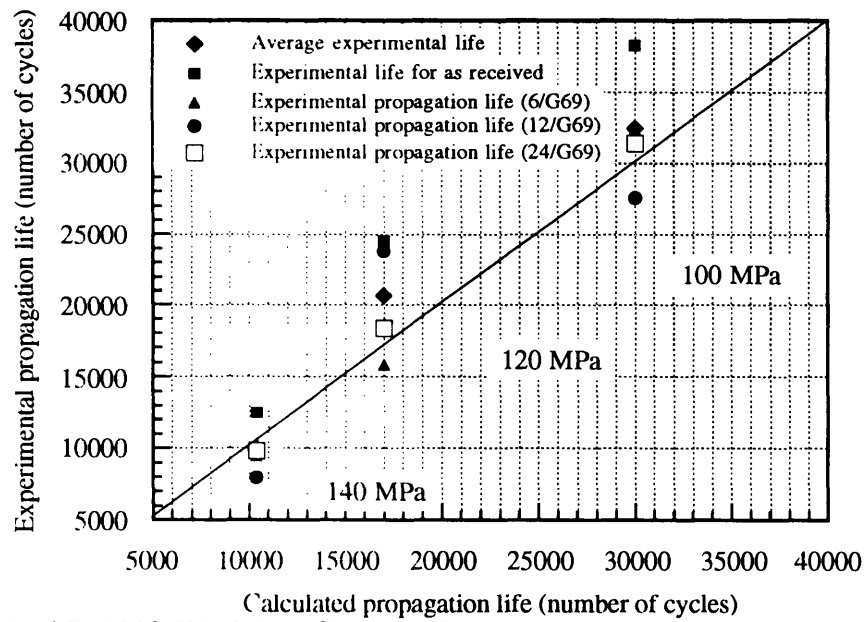
Fig.6.7: 6013-T6 alclad: Calculated and experimental propagation lives.

CONCLUSIONS

1) Microstructure

6013-T6 alclad is an aluminum-copper-magnesium-silicon alloy whose strengthening precipitates are Mg_2Si. One may also find Si, $CuMgAl_2$ and $Cu_2Mg_8Si_6Al_{15}$. Large constituent ($10\mu m$) of $(Fe,Mn)_3Si_2Al_{12}$ are observed. Grain are almost equiaxed. They are slightly flattened in the rolling plane and their dimensions are $19x25\mu m$. The aluminum cladding thickness is 60-70 μm on each side.

2) Pitting behavior

6013-T6 alclad aluminum alloy in ASTM G69 solution suffers from pitting and slight intergranular corrosion. Pitting is initiated around second phase particles. Large $(Fe,Mn)_3Si_2Al_{12}$ constituent particles are cathodic with respect to the matrix. Precipitates of Mg_2Si, Si, CuMgAl2 or $Cu_2Mg_8Si_6Al_{15}$ dissolve in ASTM G69 solution. They are anodic to the matrix whose solution-potential is evaluated at -833 mV versus a 0.1 N Calomel Electrode. Intergranular corrosion follows either a very narrow path ($0.1\mu m$) or initiates as preferential pitting along the grain boundaries. The aluminum cladding protects the base metal over short distances, but cannot prevent pitting around the constituent particles and precipitates in the inside of the rivet hole. Maximum pit depth follows a power law dependence on time of exponent 0.37. Pit area fraction seems to obey a logarithmic law. Pit density is linear with time, at least in the first six hours. Pitting density is much higher than in 2024-T3 alclad in the same condition. However, pit depth is less than in 2024-T3 alclad aluminum alloy.

3) Corrosion fatigue performance

a) Fatigue crack initiation

6013-T6 alclad is inferior in fatigue performance to 2024-T3 alclad both in the as-received and in the precorroded condition. In the as-received condition, the 6013-T6

alclad specimen inferiority may be due to a thicker cladding, an unfavorable grain structure or a lower tensile strength. In the precorroded condition, the pitting effect on fatigue crack initiation life of 6013-T6 alclad is predominant since the cladding is not seriously damaged and the fatigue crack initiation lives are severely decreased.

The higher sensitivity to corrosion of 6013-T6 alclad compared to 2024-T3 alclad may be explained by a higher pit density. Because pits are more numerous in 6013-T6 alclad, the probability of finding a critical pit on the chamfer is higher than in 2024-T3 alclad and the precorrosion sensitivity is higher. The relatively little effect of precorrosion time extension on fatigue lives may be attributed to the fact that the stress intensity at the tip of a pit varies very little with pit depth at a given pit diameter. In 6013-T6 alclad, pit depth increases much faster than pit diameter (Fig.3.3-3.4). This pitting behavior maintains a stress intensity factor at the bottom of the pits which is relatively independent from precorrosion times. It also explains why a sharp decrease in fatigue performance is observed in the early stages of precorrosion.

Corrosion fatigue crack initiation for 6013-T6 alclad in ASTM G69 is driven not only by stress concentration at the tip of the pits but by a synergistic effect between the environment and the deformation such as anodic dissolution coupled with localized plasticity.

b) Crack propagation

Crack growth rates of 2024-T3 alclad and 6013-T6 alclad are comparable in air. Precorrosion does not affect 6013-T6 alclad crack growth rates. 6013-T6 alclad crack growth rates in ASTM G69 are enhanced by a factor of 2 at low ΔK. Reducing the frequency from 10Hz to 0.1Hz does not enhance crack growth rates. Extensive crack blunting and crack branching is believed to occur and thereby it reduces the stress intensity factor at the tip of the crack.

c) Fatigue lives

It is difficult to predict fatigue lives in 6013-T6 alclad by assuming that pits act as through cracks. Calculations show that there is an induction time derived from the comparison of calculated fatigue lives with experimental total fatigue lives. In addition, there is a significant scatter. However, pits do have a detrimental on fatigue lives.

RECOMMENDATIONS FOR FUTURE WORK

1. Single sheet open hole or precracked specimen were used in this study. These specimens do not represent the lap slice joint used in the airplanes. A riveted assembly with a second aluminum sheet and an epoxy bond should be tested in the as-manufactured condition and after corrosion exposure.

2. The effect of precorrosion should be studied further since it appears that pit aspect ratios may play an important role in fatigue crack initiation. A particular emphasis should be placed on the phenomenon of fatigue performance degradation as it is related to the early stages of corrosion.

3. The real life environments should be used for accelerated tests since the ASTM G69 solution may be too corrosive, which leads to artifacts such as crack tip branching and blunting.

Stress range (MPa)	Fatigue life	As received/ in air	6/G69 in air	12/G69 in air	24/G69 in air	As received in G69
100 MPa	Initiation life	73968	36340	30890	34000	15606
	propagation life	38286	32379	27587	31402	17891
	Total life	112254	68719	58477	65402	33497
120 MPa	Initiation life	48537	29199	20625	20000	12200
	Propagation life	24508	15825	23812	18351	10852
	Total life	73045	45024	44437	38351	23052
140 MPa	Initiation life	32926	15900	13200	16000	9400
	Propagation life	12500	9508	7986	9851	5009
	Total life	45426	25408	21186	25851	14409

Table A.1: 6013-T6 alclad LT, f=10Hz, RT, R=0.05: Initiation, propagation and total lives in number of cycles as a function of $\Delta\sigma$ and precorrosion time in ASTM G69. Chamfer hole.

Stress range (MPa)	Fatigue life	As received/in air	6/G69 in air	12/G69 in air
103.6	Initiation life	135000	-	-
	Propagation life	30420	-	-
	Total life	165420	-	-
120.57	Initiation life	80000	80278	37623
	Propagation life	53299	38412	31228
	Total life	133299	118690	68851
137.8	Initiation life	48000	26720	18127
	Propagation life	13277	18819	24967
	Total life	61277	45539	43094
172.3	Initiation life	18860	11364	14938
	Propagation life	6270	10257	10340
	Total life life	25130	21621	25278
206.7	Initiation life	8300	5876	5196
	Propagation life	2531	4199	5099
	Total life	10831	10075	10295
241.2	Initiation life	2300	-	-
	Propagation life	1839	-	-
	Total life	4139	-	-

Table A.2: 2024-T3 alclad LT, f=10Hz, RT, R=0.05: Initiation, propagation and total lives in number of cycles as a function of $\Delta\sigma$ and precorrosion time in ASTM G69. Tested in air. Chamfer hole. Data processed from D.Steul MIT thesis [45]

Sress range	Number of cycles	As received/in air	6/G69 in air	As received in G69
85.6 MPa	N initiation	_	_	88390
	N propagation	_	_	30490
	N total	378000	_	118880

103.6 MPa				
test 1	N initiation	92500	39157	_
	N propagation	23560	42786	_
	N total	116060	81943	_
test 2	N initiation	_	38500	_
	N propagation	_	26157	_
	N total	_	64657	_

120.57 MPa				
test 1	N initiation	66350	30353	33000
	N propagation	13540	19873	8460
	N total	79890	50226	41460
test 2	N initiation	_	26677	_
	N propagation	_	19420	_
	N total	_	46097	_
test 3	N initiation	_	16000	_
	N propagation	_	13290	_
	N total	_	29290	_

172.3 MPa	N initiation	13390	8000	_
	N propagation	3580	2500	_
	N total	16970	10500	_

216 MPa	N initiation	4710	3500	3480
	N propagation	540	440	370
	N total	5250	3940	3850

Table A.3: 6013-T6 alclad: initiation, propagation and total lives
Straight hole, RT, f=10Hz, R=0.05

Table A.4: 6013-T6 alclad: Crack growth rate. As received. In air, R=0.05, f=10Hz, RT.

N(cycles)	ΔK (MPa√m)	da/dN (mm/cycle)
25650	5.5165	2.00E-05
32200	5.5496	1.86E-05
37000	5.5776	1.82E-05
41000	5.6006	1.90E-05
45000	5.6235	1.87E-05
51300	5.6595	2.03E-05
55000	5.6839	2.06E-05
63000	5.7297	2.09E-05
71000	5.7887	2.32E-05
81000	5.8636	2.33E-05
90000	5.9306	2.33E-05
96820	5.9787	2.36E-05
105630	6.045	2.30E-05
108500	6.061	2.71E-05
110600	6.0792	2.69E-05
112400	6.0978	2.84E-05
115730	6.1247	2.62E-05
118520	6.1448	2.55E-05
121430	6.1676	2.78E-05
124440	6.1955	2.83E-05
128000	6.2274	2.95E-05
130000	6.2474	3.02E-05
135200	6.2957	3.09E-05
138490	6.3264	3.12E-05
142000	6.3616	3.07E-05
148000	6.4225	3.20E-05
150000	6.4403	3.45E-05
154000	6.4857	3.64E-05
156000	6.5067	3.70E-05
160000	6.5574	3.95E-05
164000	6.6133	3.90E-05
166000	6.637	3.92E-05
168005	6.6607	3.91E-05
170000	6.6852	4.03E-05
173000	6.7221	4.26E-05
176000	6.7671	4.75E-05
180000	6.8348	4.64E-05
182000	6.8669	4.65E-05
184000	6.8965	4.70E-05
188000	6.9528	4.53E-05
190000	6.9839	4.35E-05
195500	7.0642	4.64E-05
199000	7.1216	4.89E-05

Table A.4(cont): 6013-T6 alclad: Crack growth rate. As received. In air, R=0.05, f=10Hz, RT.

N(cycles)	ΔK (MPa√m)	da/dN (mm/cycle)
203000	7.1872	5.19E-05
206600	7.2512	5.43E-05
208000	7.2778	5.36E-05
210000	7.3192	5.83E-05
214000	7.3957	5.60E-05
220000	7.5116	5.63E-05
223000	7.5678	6.00E-05
226400	7.6413	6.23E-05
230500	7.7342	6.60E-05
234000	7.8233	6.78E-05
237500	7.9133	7.00E-05
239000	7.9549	6.94E-05
242200	8.0333	6.77E-05
244000	8.0802	7.13E-05
246000	8.1344	7.28E-05
248000	8.1928	7.16E-05
250000	8.2468	7.14E-05
252000	8.3056	7.29E-05
254000	8.3623	7.29E-05
255000	8.3879	7.21E-05
256000	8.4158	7.55E-05
258000	8.4824	7.78E-05
259000	8.5116	7.76E-05
260000	8.5424	8.08E-05
261000	8.5759	8.45E-05
262200	8.6186	8.57E-05
263000	8.6457	8.57E-05
264000	8.6839	9.02E-05
265000	8.7211	8.96E-05
266000	8.7584	8.59E-05
267000	8.7954	8.21E-05
268000	8.8275	8.64E-05
269000	8.8635	8.45E-05
270000	8.8966	9.07E-05
271000	8.9382	9.46E-05
272000	8.9836	9.84E-05
273000	9.0268	1.03E-04
274000	9.0694	1.01E-04
275000	9.1182	1.04E-04
276000	9.162	9.93E-05
277000	9.2077	1.05E-04
278000	9.2586	9.76E-05

Table A.4 (cont): 6013-T6 alclad: Crack growth rate. As received. In air, R=0.05, f=10Hz, RT.

N(cycles)	$\Delta K(MPa\sqrt{m})$	da/dN(mm/cycle)
279000	9.2974	9.41E-05
280000	9.3386	9.62E-05
281500	9.4047	1.01E-04
282500	9.4505	1.06E-04
283500	9.5	1.07E-04
284500	9.5624	1.09E-04
285500	9.6091	1.04E-04
286500	9.6547	1.08E-04
287500	9.7078	1.08E-04
288500	9.7615	1.08E-04
290000	9.8475	1.07E-04
291000	9.9009	1.15E-04
292000	9.9546	1.20E-04
293000	10.0219	1.17E-04
294000	10.0821	1.24E-04
295000	10.1413	1.25E-04
300000	10.4946	1.41E-04
301000	10.5668	1.52E-04
302000	10.6524	1.46E-04
303000	10.75	1.52E-04
304000	10.8273	1.39E-04
305000	10.8989	1.32E-04
307840	11.1302	1.47E-04
310200	11.3592	1.62E-04
312270	11.5952	1.69E-04
314160	11.8117	1.91E-04
315670	12.0191	2.02E-04
317250	12.2438	2.18E-04
319720	12.6826	2.48E-04
320960	12.9497	2.66E-04
322520	13.3314	2.72E-04
323370	13.5324	2.73E-04
324750	13.895	2.92E-04
326490	14.3916	3.26E-04
327170	14.6198	3.64E-04
328220	15.0343	4.21E-04
329370	15.6395	5.50E-04

Table A.5: 6013-T6 alclad: Crack growth rate. Precorroded 6 hours. In air, R=0.05, f=10Hz, RT.

N (cycles)	ΔK (MPa√m)	da/dN (mm/cycle)
201300	5.013	1.00E-05
225900	5.1091	1.06E-05
252200	5.22	1.18E-05
278600	5.3431	1.27E-05
303630	5.462	1.37E-05
342560	5.6505	1.46E-05
396650	5.9462	1.72E-05
418500	6.0653	2.00E-05
447000	6.2724	2.47E-05
470000	6.4539	2.79E-05
531000	7.2012	4.34E-05
550000	7.5124	5.02E-05
570000	7.914	5.92E-05
580620	8.1473	6.50E-05
591500	8.4228	7.28E-05
605000	8.844	8.29E-05
609800	9.0177	8.62E-05
616320	9.2637	9.26E-05
622680	9.5275	9.74E-05
627100	9.7246	1.05E-04
631160	9.9176	1.10E-04
639000	10.3622	1.24E-04
643770	10.6863	1.26E-04
648400	10.9818	1.41E-04
652400	11.2805	1.55E-04
660000	12.0122	1.96E-04
665140	12.713	2.45E-04
667300	13.0912	2.63E-04
669090	13.5062	2.57E-04
671050	13.9027	2.56E-04
672400	14.1167	2.90E-04
674510	14.6776	3.50E-04
676760	15.4362	4.72E-04
678650	16.5127	6.41E-04
680070	17.7918	8.37E-04
681070	19.2402	1.05E-03
681510	19.9928	1.48E-03

Table A.6: 6013-T6 alclad: Crack growth rate. Precorroded 12 hours. In air, R=0.05, f=10Hz, RT

N(cycles)	ΔK (MPa√m)	da/dN(mm/cycle)
227800	5.13E+00	1.00E-05
247850	5.19E+00	1.09E-05
261000	5.25E+00	1.13E-05
350160	5.65E+00	1.46E-05
360000	5.70E+00	1.54E-05
376800	5.79E+00	1.64E-05
396550	5.93E+00	1.48E-05
421300	6.04E+00	1.74E-05
430000	6.08E+00	2.03E-05
441800	6.17E+00	2.16E-05
457600	6.29E+00	2.44E-05
483430	6.56E+00	3.10E-05
500000	6.77E+00	2.92E-05
504300	6.79E+00	3.29E-05
513720	6.90E+00	3.49E-05
525110	7.04E+00	3.97E-05
539500	7.27E+00	4.65E-05
544600	7.36E+00	4.72E-05
551450	7.49E+00	5.07E-05
560100	7.64E+00	5.27E-05
571150	7.87E+00	5.72E-05
574440	7.94E+00	6.07E-05
578200	8.03E+00	6.19E-05
583630	8.16E+00	6.62E-05
591400	8.37E+00	6.89E-05
598600	8.57E+00	7.35E-05
601500	8.65E+00	7.54E-05
605130	8.76E+00	7.84E-05
609920	8.93E+00	8.31E-05
615200	9.12E+00	8.43E-05
619270	9.27E+00	8.54E-05
626600	9.54E+00	8.70E-05
633300	9.80E+00	9.11E-05
637450	9.98E+00	9.29E-05
645500	1.04E+01	9.99E-05
651400	1.06E+01	1.13E-04
656700	1.10E+01	1.22E-04
664580	1.15E+01	1.44E-04
673200	1.24E+01	1.84E-04
678260	1.30E+01	2.12E-04
681040	1.35E+01	2.30E-04
683640	1.40E+01	2.61E-04
685200	1.44E+01	2.78E-04

Table A.6 (cont): 6013-T6 alclad: Crack growth rate. Precorroded 12 hours. In air,
R=0.05, f=10Hz, RT

N(cycles)	ΔK(MPa√m)	da/dN(mm/cycle)
687220	1.49E+01	3.10E-04
688440	1.52E+01	3.44E-04
690490	1.60E+01	4.28E-04
691400	1.64E+01	5.14E-04
692730	1.73E+01	6.64E-04

Table A.7: 6013-T6 alclad: Crack growth rate. Precorroded 24 hours. In air, R=0.05,
f=10Hz, RT

N(cycles)	ΔK (MPa√m)	da/dN(mm/cycle)
167720	5.10E+00	1.00E-05
189050	5.16E+00	1.09E-05
210580	5.25E+00	1.20E-05
233600	5.36E+00	1.36E-05
260160	5.50E+00	1.51E-05
278560	5.60E+00	1.62E-05
310840	5.79E+00	1.81E-05
327200	5.90E+00	1.97E-05
349170	6.06E+00	2.24E-05
373600	6.25E+00	2.55E-05
388060	6.39E+00	2.80E-05
410350	6.62E+00	3.28E-05
420010	6.73E+00	3.54E-05
428300	6.83E+00	3.78E-05
453600	7.21E+00	4.68E-05
461700	7.35E+00	4.92E-05
478700	7.68E+00	5.41E-05
489020	7.90E+00	5.90E-05
496140	8.06E+00	6.59E-05
500970	8.16E+00	6.79E-05
508770	8.39E+00	7.64E-05
520000	8.77E+00	8.55E-05
524600	8.93E+00	9.01E-05
529350	9.11E+00	9.68E-05
533350	9.27E+00	1.03E-04
538060	9.50E+00	1.12E-04
541880	9.70E+00	1.17E-04
545560	9.91E+00	1.25E-04
548200	1.01E+01	1.30E-04
552980	1.04E+01	1.37E-04
556600	1.06E+01	1.45E-04
559850	1.09E+01	1.56E-04
563410	1.12E+01	1.70E-04
566300	1.15E+01	1.81E-04

Table A.7 (cont): 6013-T6 alclad: Crack growth rate. Precorroded 24 hours. In air,
R=0.05, f=10Hz, RT

N(cycles)	ΔK(MPa√m)	da/dN(mm/cycle)
568690	1.17E+01	1.94E-04
571690	1.21E+01	2.15E-04
575500	1.27E+01	2.45E-04
580050	1.36E+01	3.14E-04
581250	1.39E+01	3.44E-04
583020	1.44E+01	4.01E-04
585230	1.52E+01	4.91E-04
586400	1.59E+01	5.70E-04
587510	1.66E+01	6.79E-04
588010	1.70E+01	7.70E-04
588840	1.79E+01	9.92E-04
589410	1.87E+01	1.30E-03

Table A.8 : 6013-T6 alclad: Crack growth rate. As received. In ASTM G69, R=0.05,
f=10Hz, RT

N(cycles)	ΔK (MPa√m)	da/dN (mm/cycle)
165800	6.08E+00	8.00E-05
171650	6.26E+00	8.58E-05
176200	6.37E+00	8.07E-05
181560	6.52E+00	8.72E-05
186400	6.69E+00	9.42E-05
192460	6.90E+00	9.58E-05
196000	7.02E+00	1.01E-04
200750	7.19E+00	1.03E-04
204600	7.33E+00	1.10E-04
210620	7.57E+00	1.19E-04
218510	7.96E+00	1.35E-04
222200	8.15E+00	1.45E-04
228200	8.50E+00	1.61E-04
233120	8.87E+00	1.64E-04
237400	9.21E+00	1.82E-04
240900	9.52E+00	2.00E-04
247000	1.01E+01	2.22E-04
252000	1.07E+01	2.28E-04
255000	1.10E+01	2.43E-04
258300	1.15E+01	2.80E-04
261400	1.20E+01	3.10E-04
262730	1.23E+01	3.26E-04
263500	1.24E+01	3.40E-04
266290	1.32E+01	3.91E-04
268730	1.39E+01	4.94E-04
269570	1.42E+01	5.21E-04

99

Table A.8(cont) : 6013-T6 alclad: Crack growth rate. As received. In ASTM G69, R=0.05, f=10Hz, RT

N(cycles)	ΔK(MPa√m)	da/dN(mm/cycle)
271590	1.53E+01	6.96E-04
272290	1.58E+01	7.79E-04
273030	1.65E+01	8.69E-04
274020	1.76E+01	1.10E-03
274620	1.88E+01	1.35E-03
274830	1.93E+01	1.86E-03

Table A.9 : 6013-T6 alclad: Crack growth rate. As received. In air, R=0.33, f=10Hz, RT

N(cycles)	ΔK (MPA√m)	da/dN(mm/cycle)
52000	4.93E+00	2.88E-05
59600	5.02E+00	3.22E-05
65000	5.09E+00	3.47E-05
78000	5.27E+00	4.11E-05
83000	5.34E+00	4.36E-05
88000	5.43E+00	4.57E-05
95220	5.56E+00	4.83E-05
100000	5.64E+00	4.99E-05
105300	5.74E+00	5.25E-05
110000	5.82E+00	5.39E-05
119110	6.01E+00	6.11E-05
125500	6.15E+00	6.64E-05
130500	6.28E+00	7.14E-05
135700	6.41E+00	7.66E-05
145400	6.69E+00	8.55E-05
150000	6.84E+00	8.96E-05
154200	6.97E+00	9.50E-05
159000	7.14E+00	1.01E-04
163500	7.31E+00	1.07E-04
169000	7.53E+00	1.14E-04
172000	7.66E+00	1.22E-04
175800	7.84E+00	1.28E-04
180000	8.04E+00	1.36E-04
184000	8.26E+00	1.48E-04
188000	8.50E+00	1.61E-04
192000	8.77E+00	1.76E-04
196000	9.06E+00	1.93E-04
200000	9.41E+00	2.15E-04
204000	9.82E+00	2.41E-04
209170	1.05E+01	2.89E-04
211200	1.08E+01	3.08E-04
213500	1.11E+01	3.49E-04
216000	1.16E+01	4.04E-04

Table A.9(cont) : 6013-T6 alclad: Crack growth rate. As received. In air, R=0.33, f=10Hz, RT

N(cycles)	ΔK(MPa√m)	da/dN(mm/cycle)
218500	1.23E+01	5.06E-04
219600	1.27E+01	5.81E-04
220770	1.32E+01	7.12E-04
221800	1.37E+01	7.97E-04
222660	1.43E+01	9.60E-04
224000	1.57E+01	1.45E-03
224470	1.65E+01	2.05E-03

Table A.10 : 6013-T6 alclad: Crack growth rate.Precorroded 6 hours. In air, R=0.33, f=10Hz, RT

N(cycles)	ΔK(MPa√m)	da/dN(mm/cycle)
1.10E+05	5.56E+00	4.00E-05
1.24E+05	5.76E+00	4.49E-05
1.38E+05	5.98E+00	5.16E-05
1.59E+05	6.39E+00	6.40E-05
1.65E+05	6.53E+00	6.88E-05
1.73E+05	6.73E+00	7.44E-05
1.78E+05	6.88E+00	7.83E-05
1.84E+05	7.04E+00	8.24E-05
1.90E+05	7.21E+00	8.81E-05
1.98E+05	7.49E+00	9.69E-05
2.04E+05	7.70E+00	1.04E-04
2.09E+05	7.89E+00	1.12E-04
2.13E+05	8.09E+00	1.20E-04
2.19E+05	8.36E+00	1.33E-04
2.24E+05	8.65E+00	1.46E-04
2.29E+05	8.95E+00	1.62E-04
2.32E+05	9.13E+00	1.71E-04
2.35E+05	9.34E+00	1.82E-04
2.41E+05	9.86E+00	2.20E-04
2.44E+05	1.03E+01	2.47E-04
2.47E+05	1.06E+01	2.70E-04
2.50E+05	1.11E+01	3.01E-04
2.52E+05	1.14E+01	3.22E-04
2.53E+05	1.16E+01	3.39E-04
2.55E+05	1.19E+01	3.72E-04
2.56E+05	1.23E+01	4.08E-04
2.57E+05	1.25E+01	4.34E-04
2.58E+05	1.29E+01	5.04E-04
2.59E+05	1.32E+01	5.66E-04
2.60E+05	1.35E+01	6.40E-04
2.61E+05	1.44E+01	8.68E-04
2.62E+05	1.48E+01	9.71E-04

Table A.10 (cont): 6013-T6 alclad: Crack growth rate.Precorroded 6 hours. In air,
R=0.33, f=10Hz, RT

N(cycles)	ΔK(MPa√m)	da/dN(mm/cycle)
2.62E+05	1.55E+01	1.18E-03
2.63E+05	1.61E+01	1.38E-03
2.63E+05	1.69E+01	1.71E-03
2.63E+05	1.74E+01	2.03E-03
2.64E+05	1.78E+01	2.57E-03

Table A.11 : 6013-T6 alclad: Crack growth rate.Precorroded 12 hours. In air, R=0.33,
f=10Hz, RT

N(cycles)	ΔK (MPa√m)	da/dN(mm/cycle)
1.33E+05	5.21E+00	2.00E-05
1.52E+05	5.38E+00	2.57E-05
1.59E+05	5.44E+00	2.78E-05
1.64E+05	5.50E+00	2.94E-05
1.75E+05	5.62E+00	3.23E-05
1.83E+05	5.71E+00	3.53E-05
2.02E+05	5.97E+00	4.21E-05
2.16E+05	6.19E+00	4.84E-05
2.23E+05	6.31E+00	5.15E-05
2.36E+05	6.57E+00	5.82E-05
2.55E+05	6.97E+00	6.97E-05
2.59E+05	7.09E+00	7.24E-05
2.63E+05	7.19E+00	7.68E-05
2.66E+05	7.28E+00	8.14E-05
2.71E+05	7.43E+00	8.58E-05
2.74E+05	7.53E+00	8.93E-05
2.81E+05	7.77E+00	9.49E-05
2.86E+05	7.92E+00	9.93E-05
2.90E+05	8.09E+00	1.04E-04
2.96E+05	8.32E+00	1.12E-04
3.00E+05	8.53E+00	1.24E-04
3.03E+05	8.68E+00	1.30E-04
3.08E+05	8.93E+00	1.38E-04
3.10E+05	9.07E+00	1.43E-04
3.14E+05	9.29E+00	1.52E-04
3.17E+05	9.54E+00	1.60E-04
3.22E+05	9.92E+00	1.77E-04
3.24E+05	1.01E+01	1.86E-04
3.28E+05	1.05E+01	2.11E-04
3.31E+05	1.08E+01	2.35E-04
3.33E+05	1.10E+01	2.51E-04
3.36E+05	1.15E+01	2.74E-04
3.38E+05	1.18E+01	2.98E-04
3.40E+05	1.22E+01	3.27E-04

Table A.11(cont) : 6013-T6 alclad: Crack growth rate.Precorroded 12 hours. In air, R=0.33, f=10Hz, RT

N(cycles)	ΔK(MPa√m)	da/dN(mm/cycle)
3.42E+05	1.26E+01	3.97E-04
3.43E+05	1.30E+01	4.30E-04
3.45E+05	1.35E+01	5.11E-04
3.46E+05	1.39E+01	6.61E-04

Table A.12 : 6013-T6 alclad: Crack growth rate. As received. In ASTM G69, R=0.33, f=10Hz, RT

N(cycles)	ΔK(MPa√m)	da/dN(mm/cycle)
8.27E+04	5.67E+00	1.00E-04
8.55E+04	5.78E+00	1.11E-04
9.06E+04	5.99E+00	1.17E-04
9.58E+04	6.21E+00	1.24E-04
9.81E+04	6.31E+00	1.29E-04
1.03E+05	6.54E+00	1.41E-04
1.07E+05	6.72E+00	1.49E-04
1.12E+05	6.99E+00	1.63E-04
1.17E+05	7.29E+00	1.80E-04
1.20E+05	7.55E+00	1.93E-04
1.26E+05	8.00E+00	2.13E-04
1.29E+05	8.20E+00	2.27E-04
1.34E+05	8.74E+00	2.57E-04
1.37E+05	9.04E+00	2.66E-04
1.39E+05	9.29E+00	2.81E-04
1.41E+05	9.52E+00	3.06E-04
1.43E+05	9.82E+00	3.37E-04
1.45E+05	1.00E+01	3.48E-04
1.46E+05	1.03E+01	3.76E-04
1.48E+05	1.07E+01	4.14E-04
1.49E+05	1.10E+01	4.42E-04
1.51E+05	1.13E+01	4.68E-04
1.52E+05	1.16E+01	4.81E-04
1.53E+05	1.21E+01	5.16E-04
1.55E+05	1.25E+01	6.02E-04
1.55E+05	1.28E+01	5.98E-04
1.56E+05	1.31E+01	6.37E-04
1.56E+05	1.33E+01	6.83E-04
1.57E+05	1.38E+01	7.66E-04
1.58E+05	1.43E+01	8.97E-04
1.59E+05	1.47E+01	1.05E-03
1.59E+05	1.53E+01	1.26E-03
1.60E+05	1.62E+01	1.60E-03
1.60E+05	1.70E+01	1.95E-03

Table A.13 : 6013-T6 alclad: Crack growth rate. As received. In ASTM G69, R=0.33, f=0.1Hz, RT

N(cycles)	ΔK(MPa√m)	da/dN(mm/cycle)
8.78E+03	7.39E+00	1.10E-04
9.55E+03	7.42E+00	1.07E-04
1.08E+04	7.48E+00	1.10E-04
1.31E+04	7.60E+00	1.09E-04
1.37E+04	7.63E+00	1.09E-04
1.44E+04	7.67E+00	1.17E-04
1.56E+04	7.73E+00	1.24E-04
1.66E+04	7.78E+00	1.37E-04
1.74E+04	7.83E+00	1.47E-04
1.82E+04	7.90E+00	1.43E-04
1.85E+04	7.92E+00	1.38E-04
1.90E+04	7.95E+00	1.26E-04
2.16E+04	8.08E+00	1.20E-04
2.20E+04	8.10E+00	1.24E-04
2.42E+04	8.24E+00	1.35E-04
2.74E+04	8.46E+00	1.40E-04
2.79E+04	8.48E+00	1.42E-04
2.97E+04	8.60E+00	1.43E-04
3.45E+04	8.92E+00	1.78E-04
3.52E+04	8.98E+00	1.83E-04
3.61E+04	9.06E+00	2.04E-04
3.66E+04	9.11E+00	2.12E-04
3.83E+04	9.29E+00	2.00E-04
3.91E+04	9.36E+00	2.02E-04
4.05E+04	9.47E+00	1.96E-04
4.36E+04	9.76E+00	2.32E-04
4.44E+04	9.86E+00	2.15E-04
4.58E+04	1.00E+01	2.24E-04
4.65E+04	1.01E+01	2.43E-04
4.89E+04	1.04E+01	2.41E-04
5.03E+04	1.05E+01	2.51E-04
5.30E+04	1.09E+01	2.81E-04
5.39E+04	1.10E+01	2.71E-04
5.42E+04	1.11E+01	2.72E-04
5.52E+04	1.12E+01	2.85E-04
5.56E+04	1.13E+01	3.18E-04
5.60E+04	1.13E+01	3.34E-04
5.64E+04	1.14E+01	3.57E-04
5.71E+04	1.15E+01	3.34E-04
5.78E+04	1.17E+01	3.46E-04
5.95E+04	1.20E+01	3.89E-04

Table A.13 (cont): 6013-T6 alclad: Crack growth rate. As received. In ASTM G69,
R=0.33, f=0.1Hz, RT

N(cycles)	ΔK (MPa√m)	da/dN (mm/cycle)
6.25E+04	1.28E+01	5.18E-04
6.29E+04	1.29E+01	5.57E-04
6.34E+04	1.31E+01	5.58E-04
6.38E+04	1.32E+01	5.89E-04
6.41E+04	1.33E+01	6.33E-04
6.48E+04	1.36E+01	6.98E-04
6.50E+04	1.37E+01	7.15E-04
6.53E+04	1.39E+01	7.43E-04
6.57E+04	1.41E+01	8.15E-04
6.59E+04	1.42E+01	8.28E-04
6.61E+04	1.43E+01	8.53E-04
6.62E+04	1.44E+01	8.79E-04
6.64E+04	1.45E+01	9.04E-04
6.66E+04	1.46E+01	9.44E-04
6.69E+04	1.48E+01	1.08E-03
6.70E+04	1.49E+01	1.10E-03
6.71E+04	1.50E+01	1.14E-03
6.72E+04	1.51E+01	1.22E-03
6.73E+04	1.52E+01	1.14E-03
6.75E+04	1.54E+01	1.08E-03
6.76E+04	1.55E+01	1.11E-03
6.78E+04	1.57E+01	1.23E-03
6.80E+04	1.58E+01	1.62E-03
6.80E+04	1.59E+01	1.42E-03
6.81E+04	1.60E+01	1.52E-03
6.82E+04	1.61E+01	1.55E-03
6.83E+04	1.63E+01	1.47E-03
6.84E+04	1.64E+01	1.46E-03
6.88E+04	1.69E+01	2.16E-03
6.88E+04	1.71E+01	2.23E-03
6.90E+04	1.74E+01	2.23E-03
6.91E+04	1.78E+01	2.45E-03
6.93E+04	1.81E+01	2.43E-03
6.97E+04	1.92E+01	3.05E-03
6.98E+04	1.95E+01	3.72E-03
6.99E+04	2.01E+01	4.98E-03

.

References

[1]:   M.F. Kanninen, Structural integrity of aging airplanes, Springer-Verlag, p.214 (1991)

[2]:   Metals Handbook, Corrosion, Vol.13(1978)

[3]:   John.E Hatch, Aluminum properties and physical metallurgy (1984)

[4]:   Alcoa Green Letter 225: Alcoa Aluminum Alloy 6013 (1988)

[5]:   Mondolfo, Aluminum alloys: structures and properties, p.647 (1976)

[6]:   Alcoa Technical Sheet: Alcoa Aluminum Alloy 6013

[7]:   J.Chaudhuri, Y.m Tan, and A.Eftekhari, J.Materials Eng. and Performance, p.91-96 (1992)

[8]:   R.S Kaneko, L.Bakow and E.W.Lee, JOM, p.16-18 (1990)

[9]:   M.Pourbaix, Atlas of electrochemical equilibria in aqueous solution, Pergamon Press, New-York (1966)

[10]:   Uhlig, Corrosion and corrosion control, second edition (1971)

[11]:   P.M Natishan, E McCafferty and G.K Hubler, J.electrochem.Soc133,1061 (1986)

[12]:   Digby D.MacDonald, J.electrochem.Soc., 139, 3434-3449 (1992)

[13]:   Z.Szklarska-Smialowska, NACE 9, p.25-32 (1987)

[14]:   J.A.Richardson, G.C.Wood, J.electrochem.Soc, Vol.120, p193 (1973)

[15]:   J.R.Galvele, J.electrochem.Soc., 464-474 (1970)

[16]:   Z.Szklarska-Smialowska, Corrosion Science, 33, 1193-1202 (1992)

[17]:   R.G Buchheit Jr, J.P Moran and G.E Stoner, Corrosion, 46, 610-617(1990)

[18]:   T.S Srivatsan,T.S Sudarshan, G.E Bobeck, Br.Corros.J., 25, 39-45 (1990)

[19]:   M.Yasuda, F.Weinberg and D.Thomas, J.electrochem.Soc, 137, 3716-3723 (1990)

[20]:   R.Wei, FAA progress report, April 1993.

[21]:   Denny A.Jones, Principles and prevention of Corrosion, p212, Mac Millan Editor

[22]: M.Baumgartner and H.Kaesche, HMSO, London (1987)

[23]: G.H.Koch, Durability of metal aircraft structures, S. Atluri editor, p.325-331 (1992)

[24]: J.R Galvele and S.M de De Micheli, Corrosion Science, 10, 795-807 (1970)

[25]: Shantanu Maitra and G.C English, Metall. Trans. A, 13A, 161-166 (1982)

[26]: T.D burleigh, Corrosion, Vol.47, No.2, p.89-98 (1991)

[27]: C.Y.Kung and M.E Fine, Metallurgical Transactions A, Vol.10A, p.603-610 (1979)

[28]: A.Zabett and A.Plumtree, Fatigue 93, Vol.1, p421-432 (1993)

[29]: M.E Fine, C.Y Kung, M.I Fadragas and J.D Achenbach, Durability of metal aircraft structures, S. Atluri editor(1992)

[30]: X.R Wu and J.C Newman, Fatigue 93, Vol.1, p.371-376 (1993) aircraft structures, S. Atluri editor, p.298 (1992)

[31]: N.L.Person, Materials performance, p.22-26 (1975)

[32]: E.F. Smith III and D.J Duquette, " The corrosion fatigue behavior of a high purity Al-Zn-Mg-Cu alloy", Technical report to the Office of Naval Research Project No.N00014-75-C-0466 (1979)

[33]: AGARD Corrosion Handbook, NATO, Vol.1, p.169-179, (1985)

[34]: S.Suresh, Fatigue of materials, Cambridge Solid State science Series, p.369 (1992)

[35]: J.P.Chubb et al, Structural integrity of aging airplanes, Springer-Verlag, (1991)

[36]: Y.Kondo, Prediction of Fatigue Crack initiation life based on pit growth,Corrosion, Vol.45, p.7-11 (1989)

[37]: J.Bannantine, J.Comer, J.Handrock, Fundamentals of metal fatigue analysis, Prentice Hall, p128 (1990)

[38]: R.P.Gangloff, NACE 10, p.59 (1990)

[39]:   E.F.Smith et al, "Hydrogen assisted fatigue cracking of high strength aluminum alloy", Technical Report to the Office of Naval Research (1975)

[40]:   H.H.Uhlig et al, Metallurgical Transactions, p.2949-2957 (1972)

[41]:   R.P.Gangloff, Materials science and engineering, p.157-166 (1988)

[42]:   Quantitative metallography, RT. Dehoff, in "Techniques for the direct observation of structures and imperfections", Vol.2, Part 1, edited by R.R Bunshash, New-York (1968)

[43]:   ASTM G69, Annual book of ASTM standards, Metals Tests Methods and Analytical Procedures, ASTM, Philadelphia, PA (1989)

[44]:   Hugh P.Godard, The corrosion of light metals, John Smiley@son Inc (1967)

[45]:   D.Steul, The fatigue behavior of 2024-T3 aluminum aircraft fuselage skin, MIT Thesis (1992)

[46]:   ASTM E647-88a, Standard Test Method for Measurement of Fatigue Crack Growth Rates, ASTM, Philadelphia, PA (1989)

[47]:   Aluminum and aluminum alloys, ASM specialty handbook, ASM (1993)